Quenching method to prepare ultra-low loading high-entropy catalyst for furfural selectively hydrogenation at ambient temperature

Xiwei Xu [a,b,1], Hui Yang [a,1], Ren Tu [a], Shuhong Liu [a], Jingye Hu [a], Yingnan Li [a], Yan Sun [a,*]

[a] *Key Laboratory for Biobased Materials and Energy of Ministry of Education, College of Materials and Energy, South China Agricultural University, Guangzhou 510640, China*
[b] *Lingnan Modern Agricultural Science and Technology Maoming Branch of Guangdong Provincial Laboratory, Maoming 525032, Guangdong, China*

ARTICLE INFO

ABSTRACT

Herein, the quenching method was employed to prepare ultra-low loading high-entropy catalyst for highly active, chemoselective, and robust furfural hydrogenation. The metals (Pd, Pt, Ru, Mo, Zn) in the form of a complex were vacancy anchored and strongly interacted with the support (TiO_2) during the quenching and reduction process, ultimately forming the high entropy catalyst PdPtRuMoZn-TiO_2 with strong metal and support interaction (SMSI) driven encapsulated layer. Moreover, this catalyst exhibits excellent catalytic performance for furfural selective hydrogenation with 90.82% conversion and 91.3% selectivity toward furfuryl alcohol at ambient temperature. The catalytic mechanism showed that high-entropy alloy (HEA) enhanced the hydrogen dissociation and migration capacity, and adjusted the electron environment of the interface between TiO_2 and HEA, causing rich oxygen vacancies in the TiO_2 SMSI driven encapsulated layer and the reduction of the horizontal furfural adsorption configuration, resulting in high FF conversion and furfuryl alcohol selectivity. The work reported ultra-low loading high-entropy catalyst and their superior performance in bio-cellulose-derived product conversion.

1. Introduction

High entropy alloys composed of five or more elements with multiple metal sites and heat and corrosion resistance were hotly concerned in the materials and catalytic field [1,2]. Compared with traditional single-element alloy materials, high-entropy alloys (HEAs) produced various unique synergistic effects, including high confrontational entropy, lattice distortion, slow diffusion, and cocktail effect [3–5]. Especially, due to the mixing of multiple metals, the surface of HEA is highly heterogeneous, resulting in a large number of different and continuous active sites, which provide diverse sites for molecular adsorption. Therefore, high-entropy alloys with unique compositions and electronic structures are considered as a new metal catalyst with great catalytic potential [6].

At present, high-entropy alloy catalysts are widely used in the field of electrocatalysis. Generally, high-entropy alloys could achieve high selective catalytic activity by adjusting the type, composition and ratio of metal elements. For example, Zhang et al. had prepared high-entropy alloy RuFeCoNiCu, and explored its multi-site cooperative reduction of nitrogen activity. The results showed that Fe was the N_2 adsorption activation site, while Co, Cu and Ni, Ru showed superior hydrogenation activity at low over potential [7]. Li et al. synthesized ultra small high-entropy alloy nanoparticles $Pt_{18}Ni_{26}Fe_{15}Co_{14}Cu_{27}$, and verified the synergistic effect of multiple active sites in the catalysts via DFT calculations [8]. Moreover, high-entropy alloy owned huge composition space and unique multi-element mixed structure, which was beneficial for achieving the goal of high activity (composition design) and low cost (non-precious metal substitute) at the same time, and had broad application prospect in complex reactions. Particularly, high entropy alloys can fine-tune the surface adsorption sites, leading to different adsorption patterns of reactants and intermediates [9]. Therefore, catalysts with high hydrogenation activity, selectivity and stability can be obtained by constructing high-entropy alloy catalysts with multiple metals via acting synergistical role.

Moreover, the simple and controllable preparation method is the cornerstone of the application of high-entropy alloy in the field of catalysis [10]. At present, there are two main methods to prepare high-entropy alloy nanoparticles, namely, the physical method of

---

"top-down" breaking bulk materials and the chemical method of "bottom-up" reduction of metal salt precursors. Physical processing can obtain high-entropy alloy bulk materials containing five or more elements, but it is not suitable for preparing nanoparticles. The wet chemistry method can control the size, shape and configuration of nanoparticles, however, which is only suitable for preparing binary and a small amount of ternary alloy nanoparticles. Recently, researchers have made some breakthroughs in exploring precise and controllable methods for preparing high entropy nano alloys. Yao et al. developed a new two-step carbon thermal shock method to synthesize high-entropy alloy with single-phase structure [11,12]. At present, by reasonably selecting the configuration and composition of elements, the electronic structure of each element and the local geometric structure of the crystal as well as the electron transfer between each element can be adjusted, which can generate new and adjustable multiple continuous active sites under the interaction of multiple adjacent elements, and build a catalyst platform with unique performance. Moreover, Glasscott et al. developed a nanodroplet mediated electrodeposition method, which can control the composition and defect distribution of metal particles by adjusting the stoichiometric ratio of metal salts in the nanodroplets [13]. Furthermore, Ye et al. obtained activating metal oxides nano catalysts with adjustble surface composition and electronic structure via queening activated methods [14]. Different synthesis strategies and preparation processes determined the composition, particle size, structure and other characteristics of high-entropy alloy, affecting the reaction activity and catalytic path [15–18]. Therefore, clarifying the regulation rules of composition and structure of high-entropy alloy, forming a controllable construction method of multi-site high entropy catalyst, plays an important role in realizing the directional regulation of its catalytic performance.

Besides, it was accepted that oxygen vacancies (OVs) can change the electronic and chemical properties of the material surface, therefore, it was widely used in photocatalysis, electrocatalysis, thermal catalysis, energy storage, batteries, and other scientific research fields [19]. Especially, oxygen vacancies played an important impact on the physicochemical properties of the catalysts, including the electronic structure, geometry, light absorption and surface adsorption and so on. The role of OVs in the catalysts was as following [20]: (1) OVs would adjust the metal oxide electronic and the band structure via moving upward the oxide Fermi energy level and reducing the energy band width. (2) OVs can promote the conversion of excitons into carriers, accelerating surface reduction reaction. (3) As an active site, OVs can optimize the adsorption energy of reactants on the catalyst surface, reduces the reaction energy barrier, promotes the molecular activation, and synergistically acts with nearby active metal sites to promote the catalytic activity [21].

The conversion of biomass resources into value-added fuels and chemicals is important for reducing the carbon footprint of today's chemical industry [22–24]. Cellulose-derived furfural (FF) is widely recognized as a platform chemical for the synthesis of sustainable liquid fuels and chemicals such as crown ethers, adhesives, furane resins, man-made fibers, fuels, and additives [25–27]. Particularly, the selective hydrogenolysis of FF to furfuryl alcohol (FA) as bio-fuels and feed-stocks has attracted much attention. However, the selective hydrogenation for furfuryl alcohol is a serious challenge due to multiple functional groups in furfural [28–30]. It is difficult to reduce one or some functional groups selectively while retaining others. Therefore, it is needed to prepare catalysts with high conversion and selectivity for the hydrogenation of FA at mild temperature and pressure.

Herein, a new ultra-low loading high entropy alloy PdPtRuMoZn-TiO₂ catalyst (0.3 wt%) with effective activation and high chemoselectivity was synthesized via quenching and vacancy anchoring method. Moreover, the catalytic activity and selectivity of PdPtRuMoZn-TiO₂ for FF hydrogenation at room temperature was investigated. Meanwhile, the role of each metal in the high entropy alloy in adjusting FA selectivity was investigated. Furthermore, the influence of OVs in the

HEA on the conversion of FF was studied. To the best of our knowledge, this is the first time that ultra-low loading high entropy alloy (0.3 wt%) realized the FF selective hydrogenation at room temperature, which supplied a new technology to realizing the high value utilization of biomass.

2. Experimental and methods

2.1. Materials

Anatase TiO_2 (5 nm), $C_4H_6O_4Pd$ (99.9%), $MoNa_2O_4$ (99%), Citric acid (99.5%), $C_{14}H_{21}O_{15}Ru_3$ (Ru40–45%), $C_4H_6O_4Zn·2\ H_2O$ (AR, 98%), $H_{12}N_4PtCl_2·xH_2O$ (98%), $FeN_3O_9·2\ H_2O$ (AR, 98.5%) , $NiC_4H_6O_4·4\ H_2O$ (AR, 99.0%), $C_4H_6CuO_4·H_2O$ (AR, 99.0%) and $C_4H_6CoO_4·4\ H_2O$ (AR, 99.5%) were purchased from Macklin Biochemical Technology Co., Ltd.

2.2. Preparation of PdPtRuMoZn-TiO₂ catalysts

For the catalyst synthesis, 0.1 mmol $H_{12}N_4PtCl_2$, 0.1 mmol $MoNa_2O_4$, 0.1 mmol $C_{14}H_{21}O_{15}Ru_3$, 0.1 mmol $C_4H_6O_4Zn·2\ H_2O$ and 0.1 mmol $C_4H_6O_4Pd$ was dissolved in 40 mL deionized water, respectively. 20 mL Citric acid (1.67 mmol·L⁻¹) was slowly added into the mixed metal salt aqueous solution and stirred for 30 min to get the metal precursor solution. During the stirring, 500 mg Anatase TiO_2 (5 nm) was calcined at 800 °C for 30 min, then the high-temperature TiO_2 was quenched in the metal precursor solution. After 10 min stirring (300 r·min⁻¹), the solid precursor was separated via suction filtration and dried in a vacuum furnace at 105 °C overnight. After that, the quenched TiO_2 was reduced Sat 800 °C for 3 h under a 10%H_2/N_2 atmosphere (200 mL·min⁻¹). Then the obtained catalyst was named PdPtRuMoZn-TiO_2. Meanwhile, PdPtRuMoZn/TiO_2 was prepared via the same method and without the addition of citric acid to the metal precursor solution. In addition, Pd-TiO_2, PdPtRuMo-TiO_2, and PdPtRuZn-TiO_2 were prepared via the same method with different metal precursor solutions. More, PdPtRuZnMoCuNiFeCo-TiO_2 was prepared via the same method and the addition of $FeN_3O_9·2\ H_2O$, $NiC_4H_6O_4·4\ H_2O$, $C_4H_6CuO_4·H_2O$, and $C_4H_6CoO_4·4\ H_2O$ to the metal precursor solution.

2.3. Catalyst characterization

Inductively coupled plasma mass spectrometry (ICP-MS, Agilent 7700X) was employed to detect the Pd-Pt-Ru-Mo-Zn content in the catalyst. X-ray diffraction (XRD) was tested via a Rigaku Ultima-IV diffractometer with Cu Kα irradiation source (λ = 0.1542 nm) and scanning speed of 10°/min (5–80°). X-ray photoelectron spectroscopy (XPS) was recorded on a Thermo Scientific K-Alpha spectrometer with monochromatic Al K-α X-rays (1486.8 eV) at $2 × 10^{-9}$mbar, and final binding energy (BE) was calibrated basing on Standard C 1 s BE (284.8 eV). The catalyst surface structure and elemental composition was characterized by transmittance electron microscopy-energy dispersive spectroscopy (TEM-EDS, Thermo Fisher Scientific) at an operating voltage of 200 KV, and the micrographs were taken on a Talos-L120C model instrument. H_2-TPD and NH_3-TPD were tested on a Micromeritics AutoChem1-II-2920 instrument. For the H_2-TPD, the catalyst (100 mg) was pretreated at 600 °C under 10%H_2/Ar with a flow of 50 mL·min⁻¹ for 10 min with a heating rate of 10 °C·min⁻¹. After that, the treated gas was changed to pure Ar flow (a total of 50 mL·min⁻¹) for 30 min, and then it was cooled to 50 °C. Then the gas was switched to 10% H_2/Ar with a total flow of 50 mL·min⁻¹ to adsorb H_2 for 1 h. An additional purge step was carried out for 1 h at the same temperature to completely remove weakly adsorbed gas under 50 mL·min⁻¹ Ar flow. The quartz tube was then heated to 800 °C at a heating rate of 10 °C·min⁻¹ and held for 10 min, meanwhile, the desorption H_2 signal was recorded by the TPD detector. For the NH_3-TPD, 100 mg catalyst was pretreated at 300 °C for 2 h and cooled to 50 °C with pure He flow (50 mL·min⁻¹). Then, the catalyst was purged with a 30 mL·min⁻¹ NH_3/

He (10%/90%) flow for 1 h, and then pure He was swiched to remove physically adsorbed NH₃ for 30 min. Once the thermal conductivity detector (TCD) baseline was stable (30 min), the furnace was heated from 50° to 650°C at a heating rate of 10 °C·min⁻¹ in 50 mL·min⁻¹ He, and the desorption NH₃ signal was recorded by the TPD detector. Pyridine IF was carried on the instrument Bruker tensor 27 (vertex 80 v). Typically, 10 mg powder sample was taken and pressed into circular slices of 15–20 mg for backup. After fixing the sample in the in-situ cell, heat it up to 400 ℃ (40 ℃·min⁻¹), and then vacuum purify it for 2 h (350 ℃, 1 ×10⁻³ Pa), then cool the sample to room temperature and scan the spectrum as background. After adsorbing pyridine at room temperature, program the temperature to the measurement temperature (fixed point temperatures of 200 ℃ and 350 ℃ respectively) for vacuum desorption (1 ×10⁻³ Pa) for half an hour, then cool to room temperature and record the infrared spectra of the 1700–1400 cm⁻¹ wavenumber region. The in-situ furfural adsorption and hydrogenation experiments were carried on Bruke Tensor II FTIR NEXUS spectrograph. Before each experiment, the sample was washed for 1 h at 30 ℃ in 30 mL·min⁻¹ He flow. Then record the substrate, then evaporate the furfural vapor at low pressure and pass it into the adsorption cell to start the adsorption of furfural. After 10 min of adsorption, record the data, and then record the data every 5 min in 30 min. After that, the gas flow was switched to He (30 mL·min⁻¹) to remove the physically adsorbed furfural, and then record the substrate, then inject 10% H₂/He (30 mL·min⁻¹) and test the surface infrared spectrum of the sample every 2 min in 30 min

2.4. Catalytic evaluation

In a typical hydrogenation experiment, 60 mg catalysts and 1 mmol furfural were mixed with 20 mL isopropanol in a stainless-steel batch reactor. The reaction temperature was set at 30 °C with 2 MPa H₂ pressure for 3 h, while the stirring speed was 400 r·min⁻¹. After the reaction, the mixture products were separated via suction filtration, then the liquid products were collected and tested by GC-MS (Thermo Trace 1300-ISQ, Thermo Fisher Scientific, Waltham, Massachusetts, USA) equipped with an HP-5 Column (30 m × 0.25 mm ×0.25 μm).

The furfural (FF) conversion, furfuryl alcohol (FA) selectivity were calculated as follows:

$$FF \quad Conversion \quad (\%) = \frac{molar \quad of \quad reacted \quad FF}{moles \quad of \quad loaded \quad FF} \times 100\% \quad (1)$$

$$FA \quad selecvity \quad (\%) = \frac{molar \quad of \quad produced \quad FFA}{molar \quad of \quad reacted \quad FF} \times 100\% \quad (2)$$

C_{FF}: the FF conversion of the reactant at time t.

The reaction rate constant (k) of the catalyst was calculated according to the first-order reaction kinetic constant formula.

$$-\ln\left(\frac{1 - C_{FF}}{100}\right) = kt \quad (3)$$

The apparent activation energies (E_a) of the catalysts were calculated based on the Arrhenius law using Eq. (4).

$$Ink = -\frac{E_a}{RT} + InA \quad (4)$$

T: reaction temperature; k: the kinetic reaction constant at this temperature and mass of catalyst used; A: the pre-exponential factor; E_a: the apparent activation energy; R: the universal gas constant.

3. Results and discussion

3.1. Synthesis of high entropy alloy catalysts

Firstly, the ultra-low loading HEA-TiO₂ catalyst was synthesized via quenching coupled oxygen vacancies anchoring method as illustrated in Scheme1. Typically, an anatase-nano-TiO₂ was calcined at 800 °C for 30 min to obtain a high-temperature TiO₂. Subsequently, the high-temperature TiO₂ was swiftly poured into a mixed solution, which dissolved C₄H₆O₄Zn·2 H₂O, C₄H₆O₄Pd, H₁₂N₄PtCl₂·xH₂O, C₁₄H₂₁O₁₅Ru₃, MoNa₂O₄, and Citric acid. During the quenching process, the chelate formed by citric acid and different metals would be anchored by the oxygen vacancies (OVs) of the TiO₂ and formed abundant precursor particles on the TiO₂ as shown in Fig. S1. The trapping phenomenon can be attributed to the anchoring effect of oxygen vacancies to the noble metals, which derived from the metal-semiconductor contact effect that the electrochemical potentials of metal and semiconductor should be uniform after contact to meet the requirement of thermodynamic
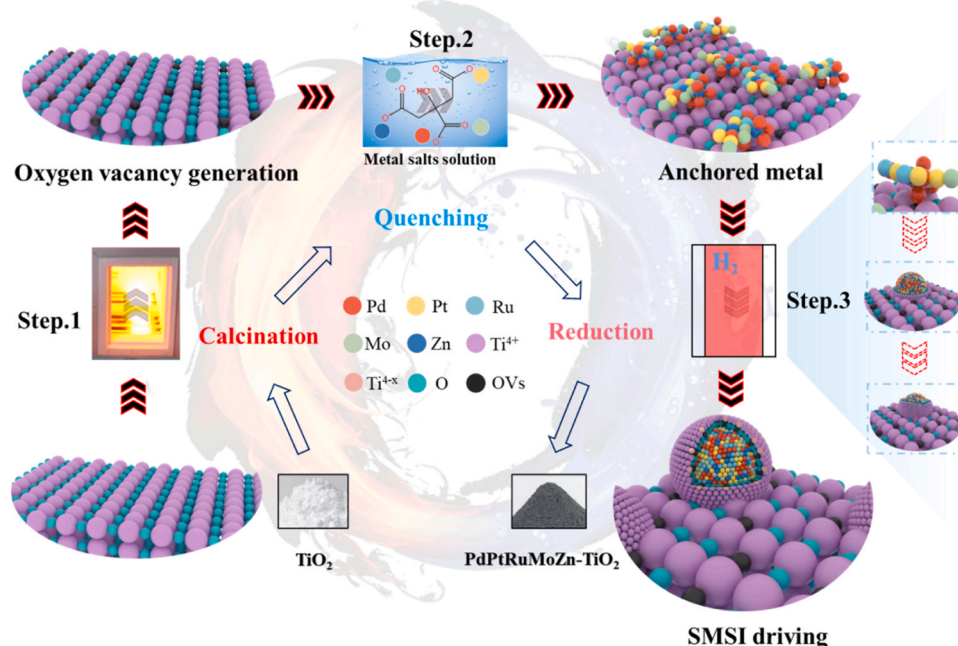
Scheme1. The synthesis procedure of ultra-low loading high-entropy catalyst.

equilibrium conditions [31]. After the quenching and anchoring process, the H$_2$ reduction (800 °C) was employed to promote the transform of chelate precursor to HEA. Meanwhile, the inducing effect of the noble metal pushed the TiO$_2$ migration to form the TiO$_x$ layer on the surface of HEA particles due to the SMSI driven during the reduction. In final, the SMSI driven encapsulated TiO$_x$ layer was obtained after 3 h reduction.

3.2. Composition and structure of high entropy alloy catalysts

To verify the structure of the prepared catalysts, TEM has been employed to observe the surface structure of the HEA-TiO$_2$ catalyst as shown in Fig. 1a. On the TiO$_2$ surface, abundant particles were dispersed evenly with an average size of around 6.89 nm. The energy-dispersive X-ray (EDX) elemental mapping image exhibits that Pd, Pt, Ru, Mo, and Zn elements dispersed in the particle uniformly, indicating that these particles consisted of the five metals. Besides, these particles exhibited a unitary lattice fringe around 0.24 nm which is different from the lattice fringe of TiO$_2$ (0.19 nm), it is worth noting that the surface of these particles was coated by a thin layer of TiO$_2$ derivative, due to the strong interaction between metal and support SMSI. It is possible that the noble metal anchored in the support successfully induced the TiO$_2$ to migrate on the surface of the particles and formed the SMSI driven encapsulated layer during the reduction, which also was keeping with our previous research. Figs. 1b and 1c also exhibited the TEM and EDS results of the PdPtRuMo-TiO$_2$ and PdPtRuZn-TiO$_2$, which showed that all these catalysts exhibited the same structural characteristic. Even though the metal numbers increased to nine, the catalyst PdPtRuZnMoCuNiFeCo-TiO$_2$ also obtained the same HEA structure. These results proved the quenching method could be proper to prepare highly dispersed nano multi-element catalysts combined with SMSI driven encapsulated layer.

Although TEM has proved that the metals were successfully loaded on the TiO$_2$, ICP was further employed to evaluate the composition of the loading metals as shown in Fig. 2a. Comparing with Pd/TiO$_2$ catalysts, it can be found that the metal loading amount showed a big difference between the two kinds of catalysts. It is accepted that molecular orbital theory shows that the new metal-O bonding orbital will have a corresponding anti-bonding orbital with higher energy than the original atomic orbital, therefore, the different metals (Pt, Pd, Ru, Mo, and Zn) would lead to different bonding strengths with semiconductor (TiO$_2$). The previous paper has proved that the occupancy state of the d orbital of Pd and the surface Oxygen atoms was more stable than the other four metals, because of the formation of stronger Pd-O bonds during the d orbital of Pd interacting with the bonding orbital of TiO$_2$ [32]. Therefore, the formation of stronger bonds (Pd-O) between TiO$_2$ and Pd made metal Pd more easily attached to the TiO$_2$ during the quenching. Limited by the original oxygen vacancy amounts, the samples showed an ultra-low metal loading amount, the Pd loading of catalyst Pd-TiO$_2$ is only around 0.3 wt%. Although the metal loading amount of the HEA-TiO$_2$ catalyst is even much lower than parts of the reported single atom catalyst, Fig. S1. shows that the precursor was attached to the TiO$_2$ in the form of nanoparticles, proving the anchoring process of the OVs attracted composite metal precursors, which may be derived from the chelation effect of the citric acid. Therefore, the ICP and TEM were employed to investigate the catalyst prepared without citric acid, while its uneven particle size distribution and disproportionate metal distribution proved the chelation effect derived by the citric acid promoted harmonious combination of metals loading on the support (Fig. S3 and Fig. S4). Since the chelation effect of the citric acid may be influenced by the properties of the metal ions, thus the metal loading of PdPtRuMo-TiO$_2$ and PdPtRuZn-TiO$_2$ were less than the Pd-TiO$_2$, indicating Pd has a higher priority level. However, even though the PdPtRuMoZn-TiO$_2$ introduced more metals to compete with Pd to adsorb on the TiO$_2$, its Pd loading was still higher than PdPtRuMo-TiO$_2$, which can be attributed to the stronger interaction between Zn and Pd promoted parts Pd to attach to Zn [33,34].

The crystalline structure of these prepared catalysts was measured by

XRD as shown in Fig. 2d. The typical diffraction peaks at 2θ = 27.4 and 36.1° corresponding to the rutile TiO$_2$ (JCPDS 34–0180), were assigned to the (1 1 0) and (1 0 1) planes, respectively. Peaks at 25.3, 36.9, 37.8, and 48.0 were assigned to the (1 0 1), (1 0 3), (0 0 4), and (2 0 0) planes, respectively, for the anatase TiO$_2$ (JCPDS 21–1272). Since the original TiO$_2$ showed a pure anatase phase, and the quenching sample also remained in the anatase phase (Fig. S5), therefore, the XRD results proved that the reduction promotes parts of the anatase TiO$_2$ to be transformed into the rutile TiO$_2$. Moreover, the peaks for HEA haven't been detected due to the fact that the content of HEA is too low (0.33 wt %) and the particle is highly dispersed. No peak indexed to an additional crystalline phase was observed, indicating that the samples maintained the basic crystalline phase after reduction treatment. However, with the increase of element types, the peak intensity and the full widths at half maximum (FWHM) of the dominant anatase peak (101) located at 25.28° gradually weaken and broaden, respectively, which also have been observed in Vignesh Kumaravel's research [35]. And they proposed that the changes should be attributed to the formation of new oxygen vacancies . Therefore, the existence of the multi-metals can induce more oxygen vacancy formation and cause lattice distortion during the quenching or reduction process, which would be beneficial for catalysts' activity.

Moreover, it should be noted that the addition of transition elements (Mo or Zn) played an important role in adjusting the catalyst. Especially, Mo promoted the transformation from anatase (TiO$_2$) to the rutile phase (Fig. 2e). It was widely accepted that phase transformation from anatase (TiO$_2$) to rutile (TiO$_2$) was due to the migration of the Ti atoms under high temperature (>900 °C) [36]. However, the addition of Mo may promote the migration of the Ti atoms at 800 °C by enhancing the interaction between the alloy particle and TiO$_2$ in the PdPtRuMo-TiO$_2$ catalyst [35]. Moreover, the addition of Zn caused a blue shift of the anatase peak (101) position (Fig. 2f). It is accepted that the blue shift of the anatase peak (101) in the PdPtRuZn-TiO$_2$ sample should be attributed to the lattice distortion that induced by the doping of smaller radius atoms, while the Zn atom radius is the smallest in the six metals (Mo (0.190 nm) > Ru (0.178 nm) > Ti (0.176 nm) > Pt (0.177 nm) > Pd (0.169 nm) > Zn (0.142 nm)). Therefore, the doping of Zn atoms should be the main reason for the anatase peak blue shift, while the subsequent lattice distortion caused by the doping is beneficial for more defect formation in the TiO$_2$ crystal structure. PdPtRuMoZn-TiO$_2$ catalyst including both transition metals showed the weakest peak intensity and the broadest FWHM, indicating HEA obtained more oxygen vacancies and the strongest interaction between the alloy particle and TiO$_2$.

3.3. Surface properties of high entropy alloy catalysts

The XRD results indicated that different loading metals showed their own effects on the catalyst structure and composition. However, limited by the ultra-low loading, the multiple-metallic particles were still hardly analyzed directly. Moreover, the structure and surface characterization of the catalyst also indicated that different metal quenching coupled reduction treatments induced the generation of surface defects. Therefore, as shown in Fig. 3a-b, a detailed oxygen defects analysis of the quenched and reduced catalysts was conducted via EPR, respectively. Notably, all the quenched catalysts showed an increase in the intensity of the EPR signal around g value= 2.0023, which represented OVs [37], compared with the TiO$_2$ sample, indicating that the quenching method is beneficial for the generation of the OVs.

Interestingly, the EPR signal intensity increased as the metal species increased. However, even though the PdPtRuMo-TiO$_2$ and PdPtRuZn-TiO$_2$ had the same metal numbers, they also exhibited different EPR signal intensity, indicating that the metal ions dissolved in water may show a different ability to promote the formation of OVs. The difference can be attributed to the different metal adsorption induced varying extent lattice distortion during the quenching process. Notably, the addition of Zn^{2+} showed a more significant effect on the formation of
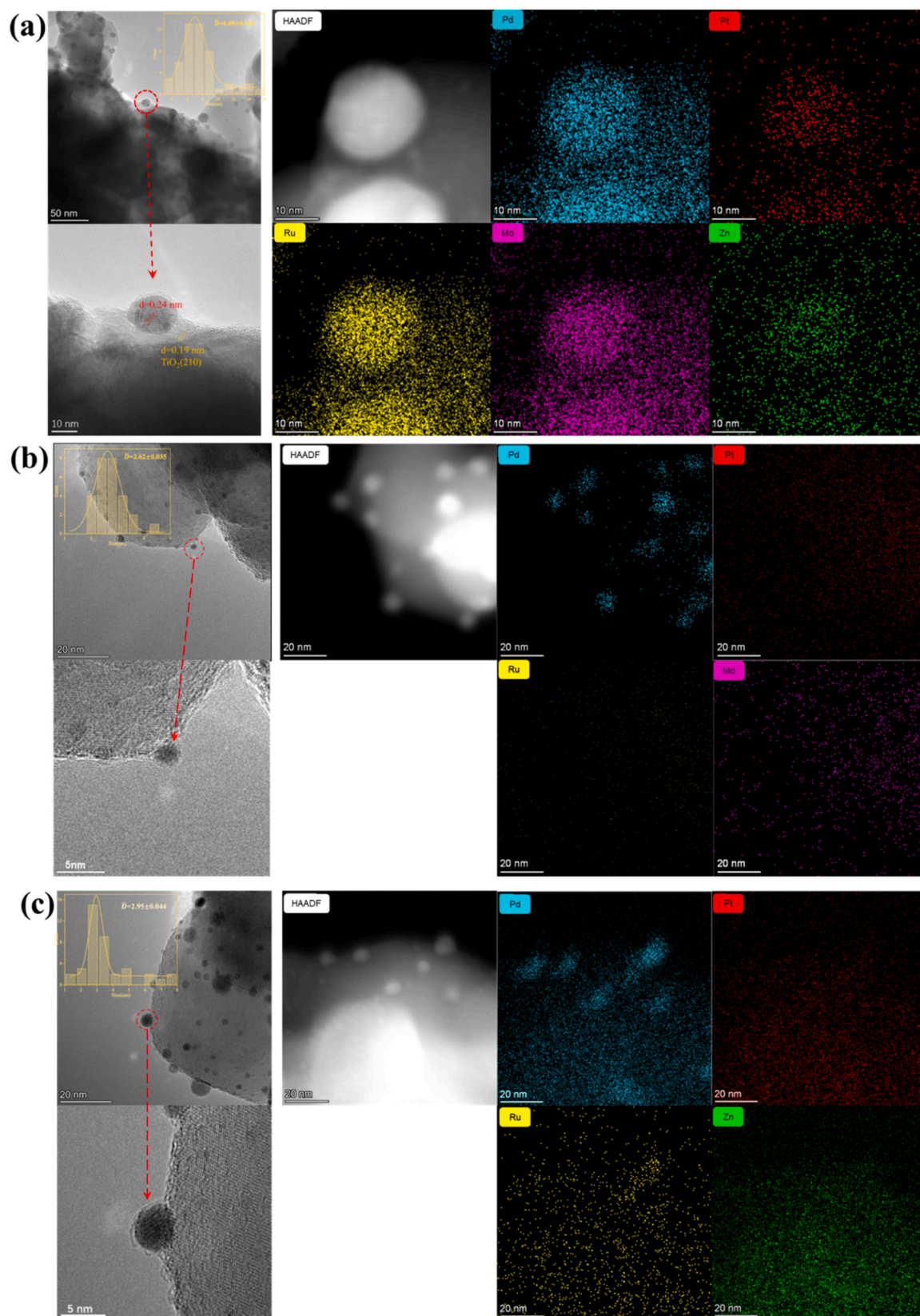
Fig. 1. The STEM-HAADF and EDS mapping of catalyst. (a) PdPtRuMoZn-TiO$_2$, (b) PdPtRuMo-TiO$_2$, (c) PdPtRuZn-TiO$_2$.
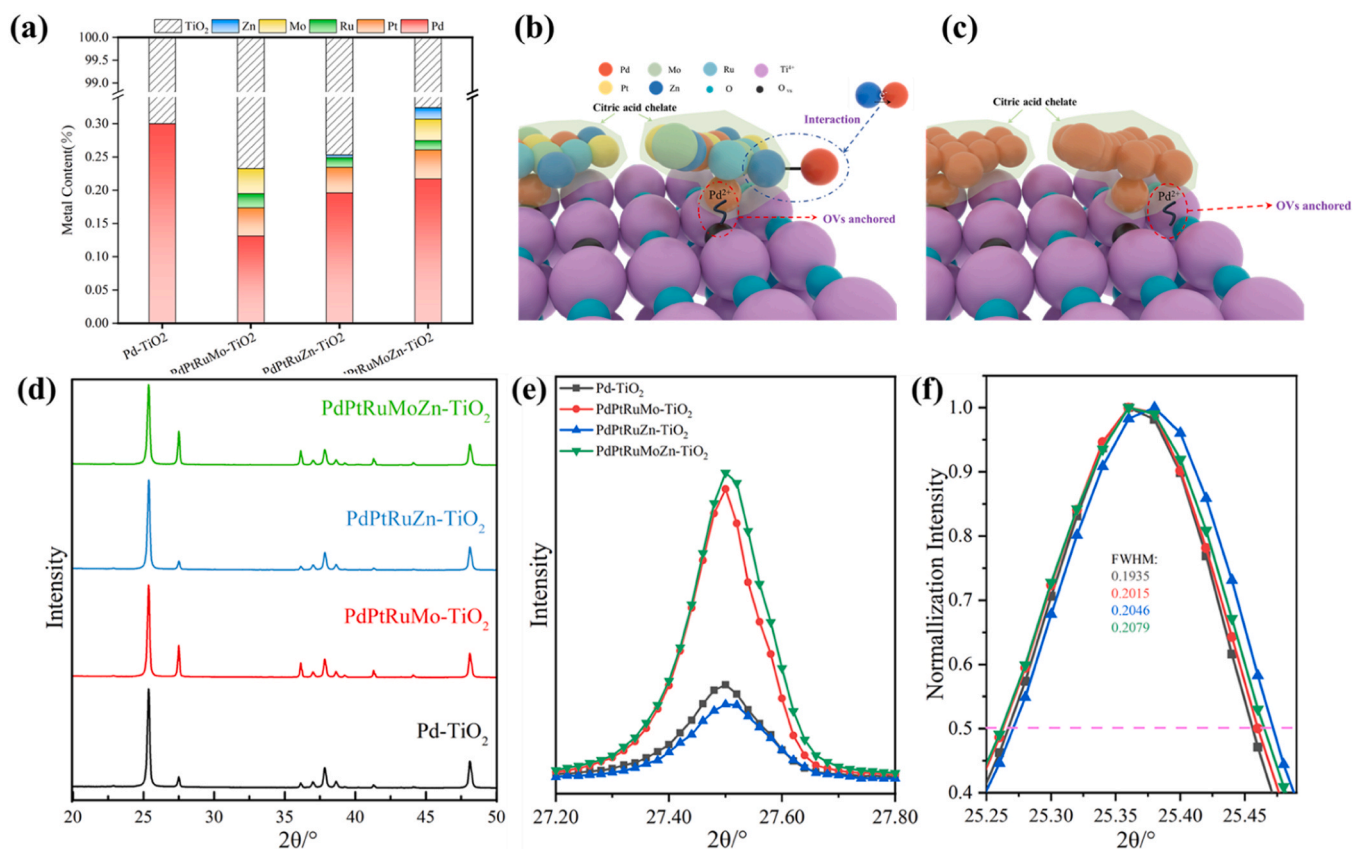
Fig. 2. (a) The ICP-OES results of catalysts, (b) and (c) Schematic of metal anchored by oxygen vacancy, (d) XRD patterns, (e) Partial magnification of XRD, (f) Normalized of XRD.
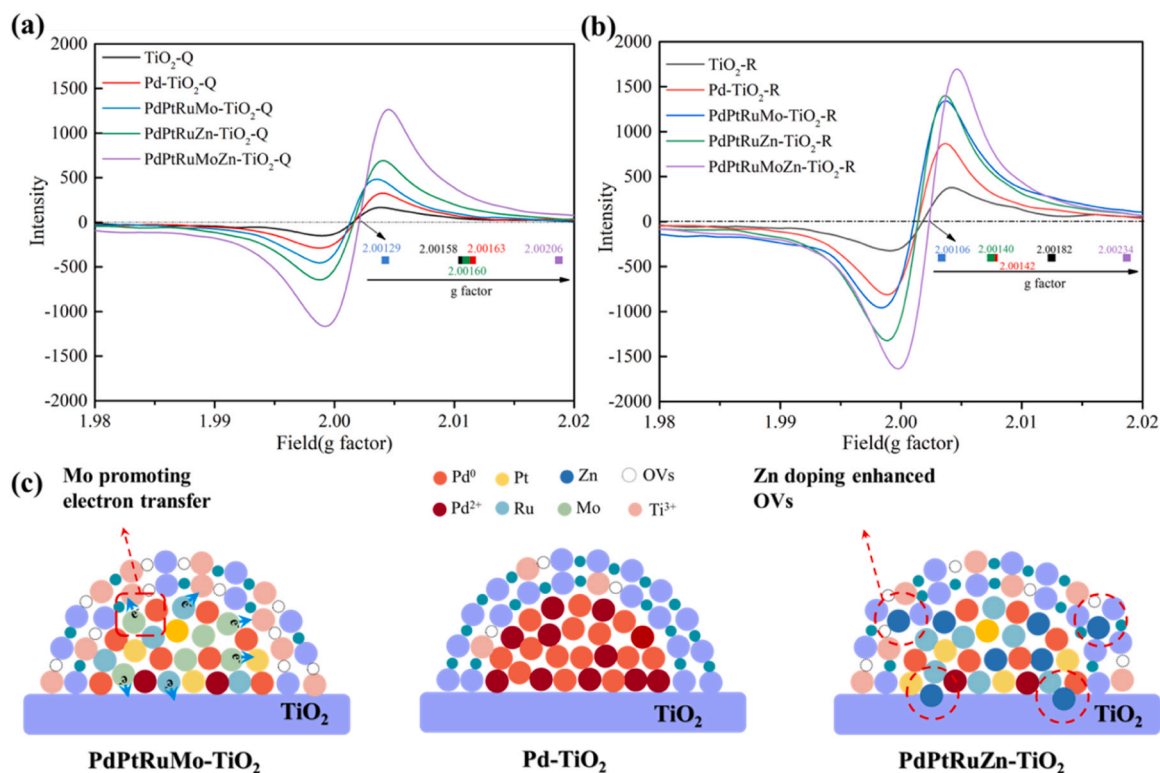

Fig. 3. EPR spectra of TiO$_2$, Pd-TiO$_2$, PdPtRuMo-TiO$_2$, PdPtRuZn-TiO$_2$ and PdPtRuMoZn-TiO$_2$ obtained at room temperature. (a) Quenching samples, (b) Reduction samples, (c) Schematic diagram of oxygen vacancy change.

OVs, which can be attributed to the doping effect of Zn^{2+} [38]. The EPR signal intensity of reduced catalysts was further enhanced compared with the quenched catalysts, proving the reduction made more surface oxygen to be removed and promoted the formation of OVs. Although the order of the EPR signal intensity of reduced catalysts kept the same as the quenched catalysts, the difference between PdPtRuMo-TiO$_2$-R and PdPtRuZn-TiO$_2$-R reduced from 25% to less than 5%, indicating the PdPtRuMo-TiO$_2$-Q obtained greater increments of the OVs during the reduction. In other words, Mo played an important role in enhancing the formation of OVs during the reduction, which is more efficient than Zn doping, indicating the two metals had different functions in adjusting the defect of the catalyst system (Fig. 3c). Moreover, the EPR signal intensity of reduced catalyst PdPtRuMoZn-TiO$_2$-R was highest, proving it obtained the most abundant OVs.

Besides the EPR signal intensity, the difference between the g values of these catalysts was also worth noting. The g value generally reflects the sum of electron spin angular momentum and orbital angular momentum, and the g value of free electron is 2.0023 because its orbital angular momentum is 0. When the vacancy electron is attracted by other atoms, its orbital angular momentum will be changed, resulting in the change of the g value. PdPtRuMo-TiO$_2$-Q showed the lowest g value in these catalysts, indicating that the vacancy electron was attracted by the other atoms, while the g value of PdPtRuMoZn-TiO$_2$-Q closed to 2.0023, suggesting its vacancy electron approached free electron. After reduction, the g value of catalysts PdPtRuMo-TiO$_2$-R, PdPtRuZn-TiO$_2$-R, and

PdPtRuMoZn-TiO$_2$-R slightly decreased, while the g value of TiO$_2$-R and PdPtRuMoZn-TiO$_2$-R increased. These results exhibited that high entropy system adjusted the electron environment between the metals, weakening the attraction for the vacancy electron. While the single metal catalyst or medium entropy system showed the opposite affection. Since OVs have been considered as the main sites for adsorbing the reactants, therefore, the amount of OVs determined the capacity of adsorbing the reactants of the catalyst, while the vacancy electron environment further determined the adsorbing strength of the reactants.

NH$_3$-TPD was employed to evaluate the acidic sites on the surface of the prepared catalysts, and the results are shown in Fig. 4a. The NH$_3$ desorption curves of all samples showed two peaks, one low-temperature peak below 200 °C and one medium-temperature peak between 200 °C and 550 °C, corresponding to the weak acid site and the medium acid site, respectively [39]. Compared with the peak area of catalyst Pd-TiO$_2$, the peak area of the other three catalysts was calculated in Fig. 4a. For the weak acid sites, PdPtRuMo-TiO$_2$ and PdPtRuMo-TiO$_2$ increased by 237% and 147% from Pd-TiO$_2$, respectively, indicating that the addition of transition elements (Mo or Zn) showed different enhancements to the weak acid site [40,41]. Moreover, the catalyst PdPtRuMoZn-TiO$_2$ obtaining the highest weak acid sites amount further indicated that HEA-TiO$_2$ catalyst combined both the assistance properties of the two transition metals. Since the main body of the catalyst was the TiO$_2$, thus the variety of the acid sites should be attributed to the TiO$_2$ structure alteration caused by metal loading.
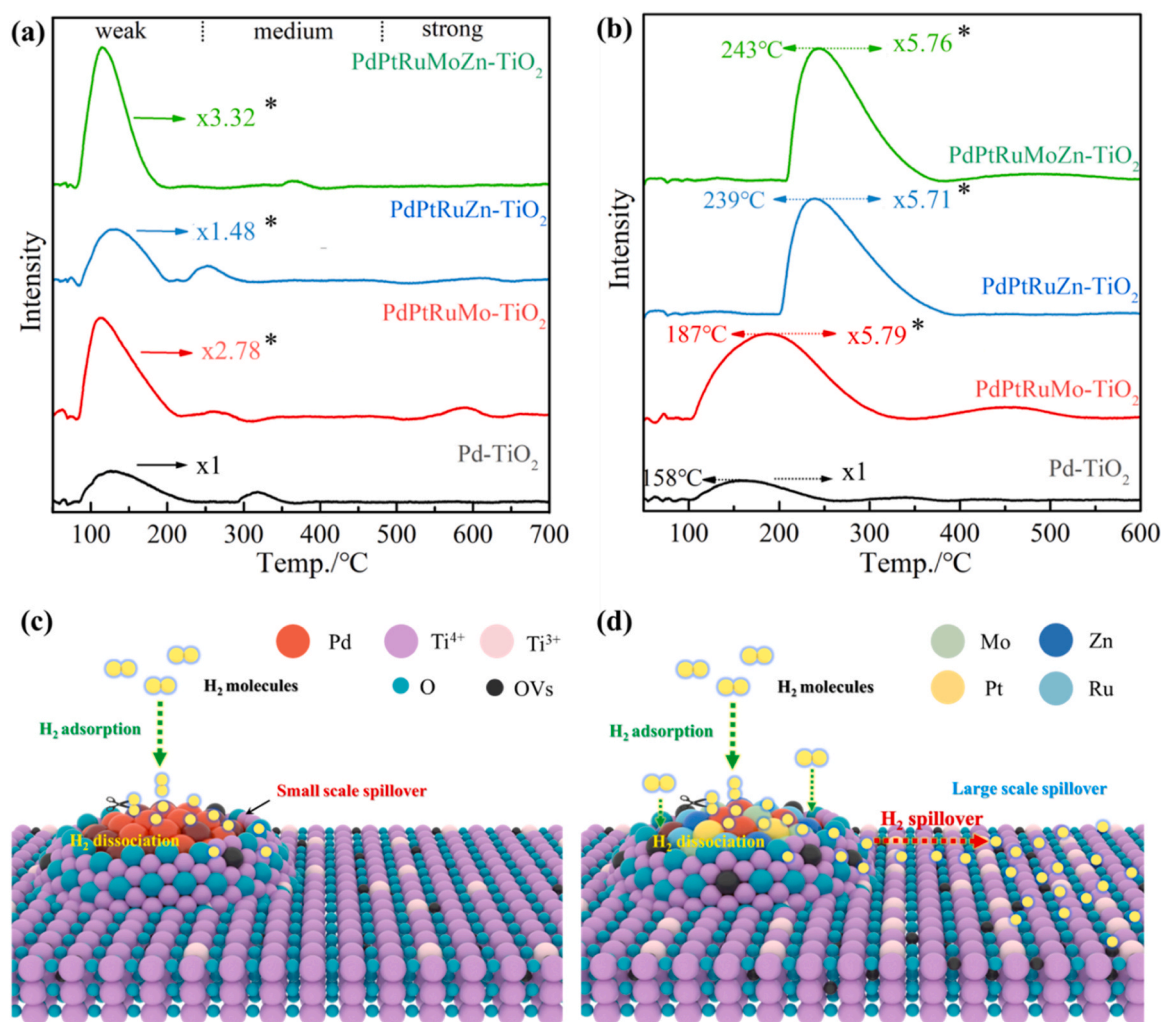

Fig. 4. (a) NH$_3$-TPD, *: the ratio of NH$_3$ desorption peak area of different catalysts to Pt-TiO$_2$. (b) H$_2$-TPD, *: the ratio of H$_2$ desorption peak area of different catalysts to Pt-TiO$_2$. (c) Pd-TiO$_2$ and (d) PdPtRuMoZn-TiO$_2$ catalyst shows a schematic diagram of the hydrogen overflow.

Pyridine adsorption IR was employed to further verify the distribution of the acidic site types in the catalysts, and the results were shown in fig. S7. it can be found that the addition of Mo slightly enhanced the Lewis acid proportion, while the addition of Zn enhanced the Brönsted acid proportion. For the catalyst PdPtRuMoZn-TiO₂, its Brönsted acid proportion increased improved by 7.3% and 5.8% comparing with PdPtRuMo-TiO₂ and PdPtRuMo-TiO₂, respectively. These results further verified that the high entropy catalyst combined the characteristics of two metals and achieves more obvious varies.

Hydrogen temperature-programmed desorption (H₂-TPD) tests of the samples were carried out to investigate the hydrogen adsorption ability and spillover effect (Fig. 4b). For the Pd-TiO₂ sample, weak H₂ desorption peaks can be found centered at 158 °C, which could be assigned to the chemisorbed hydrogen of the Pd in subsurface layers or the metal-support interface. Interestingly, although PdPtRuMo-TiO₂ showed less metal loading amount, especially the noble metals amount (Fig. 2a), was much less than the Pd-TiO₂, but it exhibited similar desorption peaks in the temperature range of 100–300 °C, while its peak intensity was much higher than that of Pd-TiO₂, suggesting that the

loading of the other three metals promoted hydrogen spillover on the catalyst [42,43]. Further, to verify the presence of hydrogen spillover on the catalyst surface, WO₃ as an indicator was mixed with HEA catalyst physically to conduct the hydrogenation reaction to investigate whether activated H* was spilled to the support. The results were shown in Fig. S8. It showed that the color was still gray yellow when only WO₃ was in hydrogenation reaction. In contrast, WO₃ +HEA catalyst was reduced visibly, while the color of WO₃ changed into bluish gray in the mixed solution, indicating the occurrence of hydrogen spillover. To investigate the reason for the enhancement of the hydrogen spillover phenomenon, the H₂-TPD results of different quaternary catalysts were compared (Fig. S6). The results exhibited that the addition of precious metals Ru and Pt can greatly improve the hydrogen capacity of the catalyst, while the addition of Mo and Zn has only a slight effect on the enhancement of hydrogen adsorption. Moreover, for the catalysts PdPtRuZn-TiO₂ and PdPtRuMoZn-TiO₂, although the peak intensity of H₂-TPD was similar with PdPtRuMo-TiO₂, their peak temperature increased from 187 °C to 239 °C and 243 °C, respectively, indicating that the strength of H₂ adsorption of both catalysts increased. Generally,
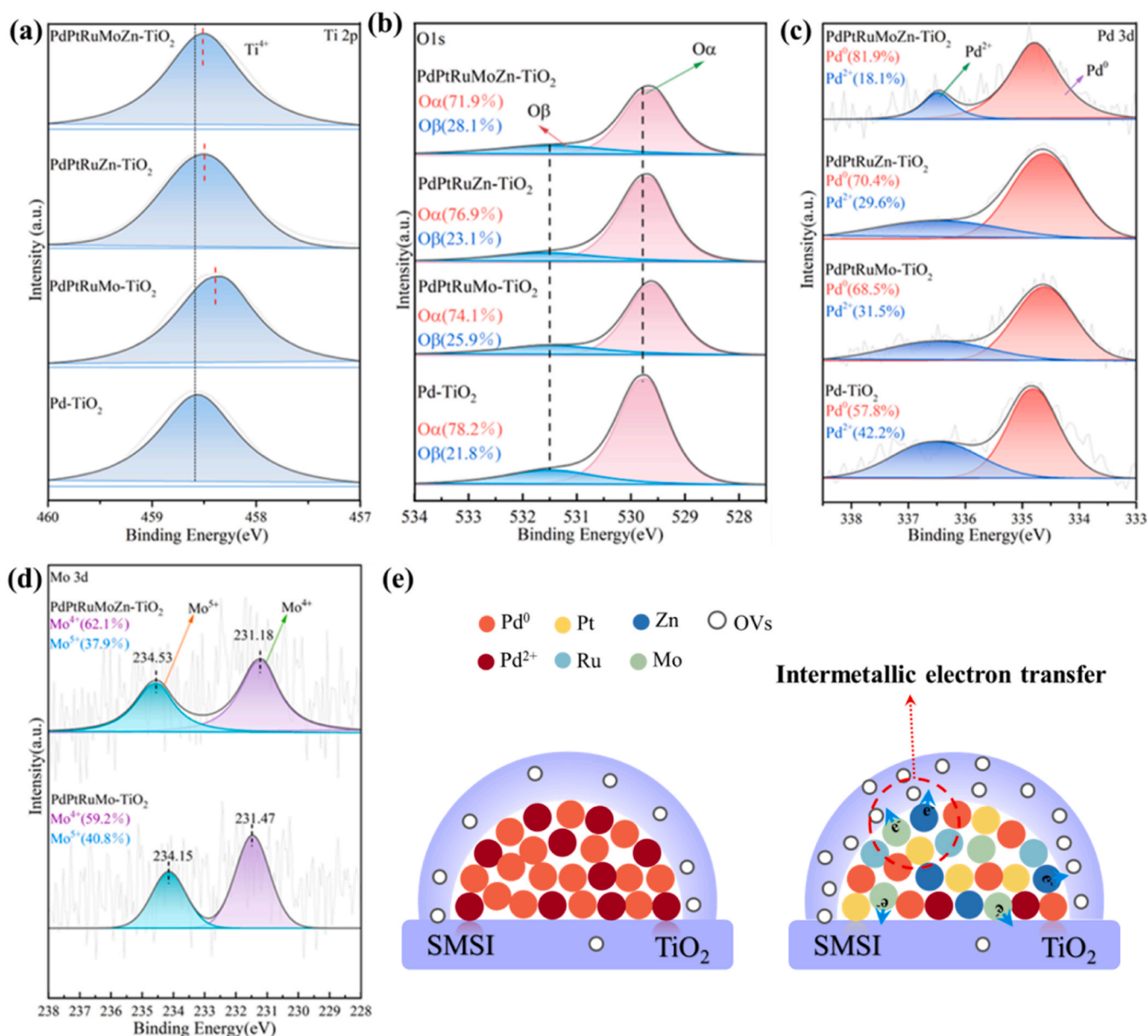

Fig. 5. (a) Ti 2p, (b)O 1 s, (c) Pd 3d, and (d) Mo 3d, (e) Schematic diagram of internal electron transfer in HEA.

the stronger hydrogen adsorption may limit its migration and inhibit the hydrogen spillover [44], but both catalysts showed a similar H_2 adsorption amount with catalyst PdPtRuMo-TiO$_2$, indicating that the enhancement of the hydrogen adsorption strength showed little influence on the hydrogen spillover. Therefore, it can be inferred that subsequent reactions will not be directly affected.

In summary, the multi-metal loading enhanced the surface hydrogen spillover and improved the adsorption intensity of the spillover hydrogen. As previous research reported, hydrogen spillover occurred via the migration of proton and electron pairs on the surface of the catalyst. Moreover, the Lewis acidic sites generated by oxygen vacancies are often accompanied by Lewis basic sites on adjacent lattice oxygen surfaces known as frustrated Lewis pairs (FLPs) [45]. And the Lewis basic sites would promote the hydrogen spillover by providing the electron pairs [46], which should be the main reason for the enhancement of the hydrogen spillover. Moreover, the enhancement of hydrogen adsorption intensity was related to the variety of hydrogen adsorption sites. Generally, the spillover hydrogen spilled from the dissociation sites to the carrier (SMSI coating layer). The addition of Zn caused changes in the surface electronic structure of the carrier, especially the SMSI coating layer, resulting in the improvement of the hydrogen adsorption strength of the dissociation site and the carrier (SMSI driven encapsulated layer).

All the catalysts with different loading metal species were characterized by XPS and the results are shown in Fig. 5. It should be noted that the metal content in the HEA catalysts is very low (<0.01 wt%), which can only give noisy spectra even after an unusually large number of scans (>100), especially the spectra of Zn (Fig. S9). Therefore, the valence state in the catalysts was compared via Ti 2p, O 1 s, Pd 3d, and Mo 3d spectra to evaluate the surface electron distribution. Previous characterizations have proved that the addition of Mo and Zn exhibited different effects on the surface electron distribution, which was also testified in XPS results. As shown in Figs. 5a and 5b, the binding energy of Ti 2p decreased from 458. 75 eV of Pd-TiO$_2$ to 458.25 eV of PdPtRuMo-TiO$_2$, while the one in PdPtRuZn-TiO$_2$ was 458.51 eV. The same phenomenon was also observed in O 1 s spectra, while PdPtRuZn-TiO$_2$ kept the same binding energy with Pd-TiO$_2$, and PdPtRuMo-TiO$_2$ obtained a lower O 1 s binding energy around 529.81 eV. These results indicated that the addition of Mo provided a novel electron-obtaining way for the O atoms of TiO$_2$, leading to the O atoms gaining some electrons from the element Mo, and then weakening the electron transport from Ti or Pd to O. Moreover, although the catalyst PdPtRuZn-TiO$_2$ also showed a lower binding energy of Ti 2p, its binding energy is still higher than PdPtRuMo-TiO$_2$, indicating that the other two noble metals (Ru, Pt) showed less effect on the electron transferring, while the Zn also showed a weaker effect on the electron transfer than Mo. However, the combination of Zn and Mo in the PdPtRuMoZn-TiO$_2$ sample even weakened the effect of Mo on the electron transfer, which may be due to the doped Zn providing a new site to receive the electron transferred from Mo.

As shown in Fig. 5b, it can be found that the XPS spectrum of O 1 s was consist with two peaks, the characteristic peak at 529 eV corresponding lattice oxygen(O_α), while the other board peak located around 531 eV corresponding oxygen defects (O_β) [47]. The proportion of each peak was calculated and listed in the Fig. 5b as well, and the results suggested that the proportion of O_β increases with the addition of Mo and Zn. However, the trend was different with the EPR findings, potentially attributable to the fact that XPS generally reflects signals from the catalyst's surface. Notably, the change in the proportion of oxygen vacancies was consistent with the trend of acid site changes (Fig. 4a). This validates the prior hypothesis, stating that the increased in oxygen vacancies had a positive impact on the enhancement of acid sites. Fig. 5c exhibits the spectra of Pd 3d, as the loading metal increased from the single Pd to the five elemental HEA PdPtRuMoZn, the proportion of Pd^{2+} decreased from 42.2% to 18.1%, meanwhile, the Pd^0 increased from 57.8% to 81.9%. It is possible that the electron transfer

between multi-metals may regulate the electron exchange interaction between Pd and external atoms. Especially, the effect of Zn doping and Mo strengthening electron transfer made it possible for them to replace parts of Pd to participate in external electron exchange. Therefore, as the number of metal elements increased, parts of Pd can exist as the formation of Pd^0, especially in PdPtRuMoZn-TiO$_2$ sample high-entropy alloy systems.

3.4. Evaluation of catalytic performance

The above results exhibited that the multiple metal loading catalyst enhanced the H_2 adsorption capability and the OVs of the catalyst, while the NPs were stably supported on the TiO$_2$ due to the SMSI effect. This feature is highly valuable in adjusting the catalytic performance. And it was applied in the hydrogenation of FF. According to previous reports, there are two major reaction steps for FF hydrogenation (Fig. 6a) [48]. Step 1 was widely considered the main route for the selective hydrogenation of FF to FA, while FA was susceptible to further hydrogenation to tetrahydrofuran alcohol (THFA) via Step 2. As shown in Figs. 6b and 6c, Pd-TiO$_2$ obtained 75.6% FA selectivity after a 2.5 h via hydrogenation reaction at 30 °C. However, the conversion of FF was as low as 42.31%. Remarkably, both PdPtRuMo-TiO$_2$ and PdPtRuZn-TiO$_2$ exhibited much higher FF conversion from 40.82% to 67.41% and from 62.21% to 76.43%, respectively, at the same reaction condition, indicating the addition of Mo and Zn improved the catalytic activity and selectivity. However, although the OVs and H_2 adsorption amount of PdPtRuMo-TiO$_2$ and PdPtRuZn-TiO$_2$ are similar, their FF conversion was different. Therefore, it can be induced that the higher g value of PdPtRuZn-TiO$_2$ catalysts may be the main reason for the its higher FF conversion. It was possible that the reactant adsorption intensity aroused by the electron distribution of OVs had a significant influence on the FF conversion as well. In addition, the highest FF conversion was obtained via the PdPtRuMoZn-TiO$_2$ catalyst reaching 90.82% due to the combination role of the five metals in HEA catalysts. On balance, the changes in the FF conversion were consistent with the results of H_2-TPD and EPR, indicating the enhancement in OVs and H_2 adsorption in HEA catalysts increased the FF conversion.

Moreover, the selectivity of the FA and THFA are different via single and multi-metal catalysts. The results demonstrated that loading metal species adjusted the route of FF hydrogenation, especially limiting the further hydrogenation of FA. As our previous research proved, the adsorption configuration of FF on the catalyst played an important role in adjusting the product selectivity. Therefore, the changes in product selectivity should be attributed to the influence of the loading metal on the FF adsorption configuration. Based on the above characterization results, the OVs can be considered the main sites for FF adsorption, while the HEA NPs played the role to adsorb and dissociate H_2. Remarkably, the SMSI effect made the HEA NPs was covered by the OVs-rich TiO$_2$-derived layers, which made it possible that the dissociated hydrogen proton spilled to the TiO$_2$-derived layers and react with the adsorbed FF by OVs. Moreover, it also provided the opportunity for the HEA NPs to participate in the FF adsorption and change the vertical adsorption configuration. XPS results have proved that the valence state of Ti and O showed a slight difference between the catalysts, while the Pd^{2+} and Pd^0 proportion exhibited a big gap in the different catalysts. Moreover, Song et. al proved Pd^{2+} was the active site for the adsorption of furnan ring in FF, therefore, it was induced that the contiguous OVs and Pd^{2+} participated in the FF adsorption, leading to a horizontal adsorption configuration of FF [49]. However, as the loading metal increased from the single Pd to a combination of PdPtRuMoZn, the proportion of Pd^{2+} decreased from 42.2% to 18.1%, which significantly reduced the occurrence of the horizontal adsorption configuration. Therefore, the selectivity of FA significantly increased via PdPtRuMoZn HEA catalysts.

The linear relationship between $-ln(1-C_{FF})$ and reaction time (t) for all catalysts was shown in Fig. S10. The hydrogenation of FF to FA can be described as pseudo-first order. Based on Eq. 3, the order of reaction
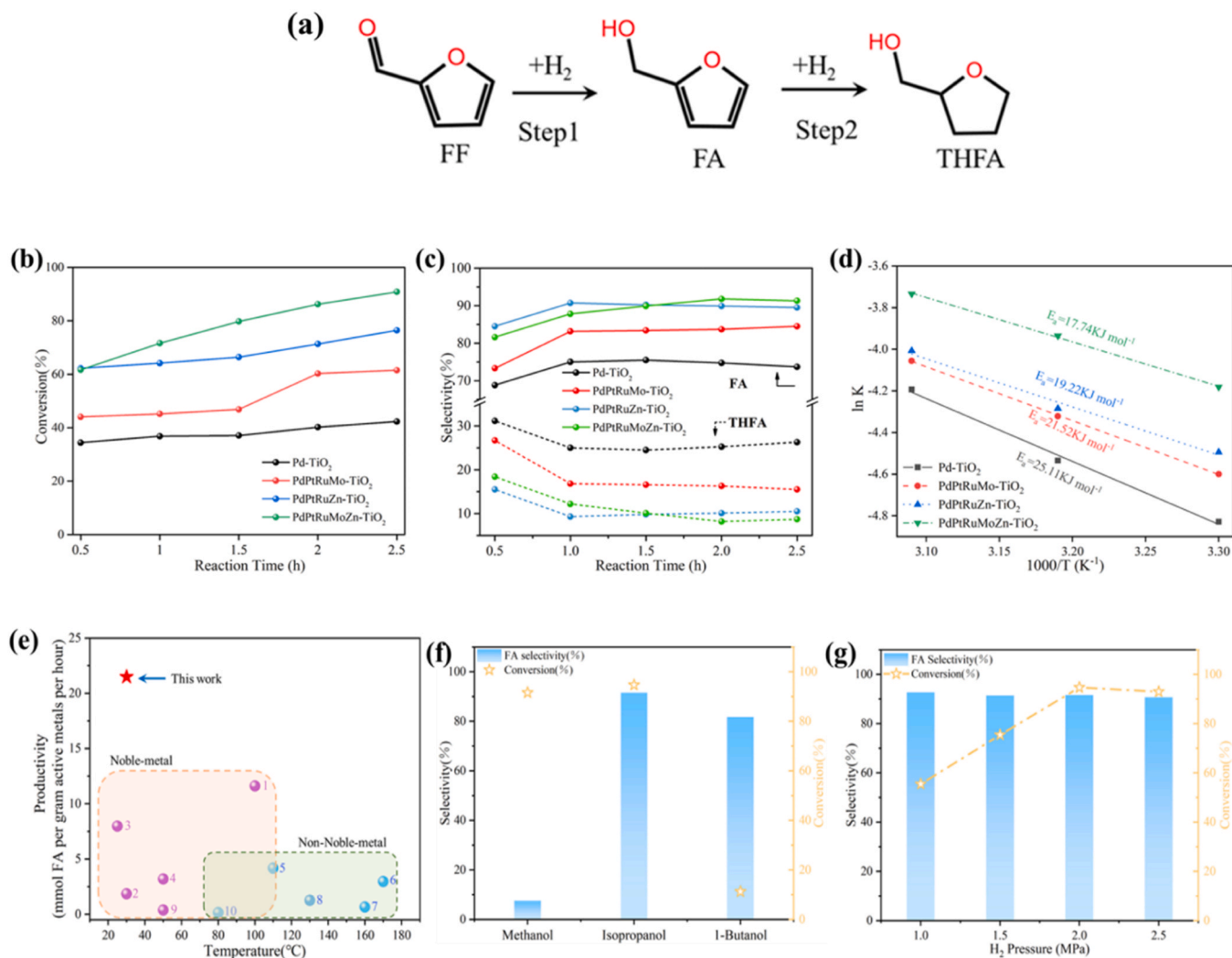
Fig. 6. (a) Reaction pathways for FF conversion to FA and THFA, Catalytic hydrogenation of FF via different catalysts (b) FF conversion with time and (c) FA selectivity with time (30 °C, 2 MPa H$_2$ and 15 min), (d) the Arrhenius regressions, (e) Comparison of the catalytic performances of the state-of-the-art catalysts for the hydrogenolysis of FF to FA. A summary of the productivities of representative noble-metal catalysts (purple circles), non-noble-metal catalysts (blue circles), this work. Full data is shown in Table. S1. (1) PtSn/SiO$_2$ [50], (2) RuPd/TiO$_2$ [51], (3) Pd$_3$Pb MF/C [52], (4) PdRe/Al$_2$O$_3$ [53], (5) CuMgA l[54], (6) CuZnCrZr [55], (7) NiCoZn@CN [56], (8) CuCoZn@NPC[57], (9) Pd/Cu [58], (10) Co@CN-G600 [59], (f) Reaction solvents (reaction conditions: 1 mmol FF, 60 mg catalyst, 20 mL of solvents, H$_2$ pressure of 2 MPa,30 °C and 2.5 h), (g) Reaction Pressures (reaction conditions: reaction conditions: 1 mmol FF, 60 mg catalyst, 20 mL of isopropanol, 30 °C and 2.5 h).

kinetic constants (k) of the catalysts is PdPtRuMoZn-TiO$_2$ > PdPtRuZn-TiO$_2$ > PdPtRuMo-TiO$_2$ > Pd-TiO$_2$. The k values of the catalysts were influenced by the addition of either Mo or Zn, and produced a more pronounced effect when combined, which proves that the activity of the catalysts can be promoted by the Mo and Zn. The apparent activation energies (Ea) of these catalysts have been calculated via numerical regression and Arrhenius' law (Fig. 6d). As a result, the catalyst Pd-TiO$_2$ showed the highest Ea (25.11 KJ·mol^{-1}), whereas the catalyst PdPtRu-MoZn-TiO$_2$ displayed the lowest Ea (17.74 KJ·mol^{-1}), indicating that the PdPtRuMoZn-TiO$_2$ catalyst obtained the best catalytic performance, which further proved the significant effect of the combination of Mo and Zn. The addition of Mo and Zn was essential to adjust electron distribution, which not only further influenced the reactant adsorption and migration, but also adjusted the adsorption configuration, resulting the FF to be transformed to FA more effectively. Meanwhile, the reaction time kinetics experiment exhibited that basic equilibrium was kept between reactant conversion and product yield, indicating that the products can be quickly desorbd from catalyst. The productivities were calculated (Fig. 6e) and importantly, PdPtRuMoZn-TiO$_2$ showed remarkably high productivities at the ambient temperature (30 °C),

outperforming all state-of-the-art metal-based catalysts including most of noble-metal-based and non-noble-metal-based catalyst reported.

Since the hydrogenation activity of the catalyst would also be influenced by the polarity of the solvent. The FF hydrogenation reaction was carried out at various solvents with the PdPtRuMoZn-TiO$_2$ catalyst. As shown in Fig. 6f, the conversion of FF followed the order of iso-propanol ≈ methanol > 1-butanol, while the FA selectivity followed the order of isopropanol ≈ 1-butanol > methanol. Although the strong polarity solvent methanol obtained the higher conversion of FF, it also promotes the formation of etherification products, indicating its strong polarity may induce the active sites being occupied and arousing the occurrence of the side reaction (etherification). However, the weak polarity solvent 1-butanol obtained higher FA selectivity, but its FF conversion was only 11.23%, exhibiting that its weak hydrogen donating effect may limit the hydrogen proton migration and hinder the hydrogenation reaction. Therefore, the medium polarity solvent iso-propanol provides a proper reaction environment to achieve effective FF selective hydrogenation. As shown in Fig. 6g, the effect of H$_2$ pressure on the hydrogenation of FF was investigated as well. The FF conversion increased from 71.40% to 90.82% with the H$_2$ pressure increasing from

1.0 MPa to 2.0 MPa, while the FA selectivity maintained around 90%. The result indicated that the amount of hydrogen proton would mainly influence the FF conversion, while its effect on the selective hydrogenation was slight. Moreover, further increasing the H_2 pressure to 2.5 MPa showed negligible effect on both FF conversion and FA selectivity, proving the adsorption configuration of FF on the PdPtRuMoZn-TiO$_2$ may limit the hydrogenation from FA to THFA.

Overall, the catalytic activity seems to be the same variety trend as the adsorption site. The relationship between the conversion of FF and EPR signal (OVs concentration) were summarized in Fig. 6 as well as the relationship of FA selectivity with the Pd^0/Pd^{2+} ratio (XPS results). As shown in Fig. 7a the FF conversion and FA selectivity showed a positive relationship with the OVs concentration and the Pd^0/Pd^{2+} ratio, respectively (Fig. 7b). As mentioned in the previous analysis, the increased OVs enhanced the hydrogen spillover on the catalyst surface, therefore, it promoted the adsorption of hydrogen and furfural at the same time, thereby improving the conversion of furfural. Moreover, the change in the valence state of Pd atoms may affect the adsorption configuration of FF on the catalyst, leading to a change in selectivity.

3.5. The analysis of the reaction mechanism

To verify the adsorption and intermediate reaction process of the FF hydrogenation reaction, we have performed two steps to investigate DRIFTS results at ambient temperatures. The first stage was that the catalyst exposed to the FF flow to adsorb the FF on the active sites, and the second stage would change the FF atmosphere to H_2 to record the adsorbed FF being hydrogenated. Since catalysts PdPtRuMoZn-TiO$_2$ and Pd-TiO$_2$ showed a significant gap in the FF conversion and FA selectivity, therefore, both the catalysts were tested in the in-situ DRIFTS experiments. As shown in Figs. 8a and 8b, the catalysts exhibited the same peaks in the in-situ DRIFTS results after absorption, the bands at 1000–1200 cm^{-1} were attributed to furan ring respiratory vibrations, while the bands at 1600–1800 cm^{-1} were attributed to carbonyl stretching vibration of FF. To better compare the FF adsorption differences in the two catalysts, we calculated the ratio of peak intensities of the two characteristic peaks (1157 cm^{-1} and 1696 cm^{-1}), and the increment of peak area (1157 cm^{-1} and 1696 cm^{-1}) with increasing adsorption time (Table. S3). For the catalyst PdPtRuMoZn-TiO$_2$, the peak area of 1157 cm^{-1} and 1696 cm^{-1} increased by 75% and 67% as the adsorption time increased from 10 min to 35 min, receptively, while the peak intensity ratio of carbonyl stretching vibration peak (1696 cm^{-1}) to furan ring respiratory vibrations peak (1157 cm^{-1}) was kept around 2.49, indicating the adsorbed FF maintained single adsorption configuration at all adsorption time. However, for the

catalyst Pd-TiO$_2$, the peak area of 1157 cm^{-1} increased by 45% as the adsorption time increased from 10 min to 30 min, while the peak area increment of 1696 cm^{-1} only increased by 11%. Moreover, the peak intensity ratio of carbonyl stretching vibration peak (1696 cm^{-1}) and furan ring respiratory vibrations peak (1157 cm^{-1}) also decreased from 4.78 to 3.65. These results proved that the adsorbed FF may exist in two adsorption configurations in the catalyst Pd-TiO$_2$. At the initial adsorption, the adsorption configuration was a horizontal adsorbed mode which co-adsorbed furan ring and carbon group, while subsequent adsorption shifted to a vertical adsorption mode which was dominated by carbon group adsorption as the adsorption quantity increased.

In the second stage, all the peaks area in the PdPtRuMoZn-TiO$_2$ decreased rapidly with the reaction time, indicating that the adsorbed FF was hydrogenated quickly and desorbed due to its excellent hydrogen adsorption and transfer capabilities. However, the peak area of Pd-TiO$_2$ showed a slowly decrease, which was also consistent with its poor hydrogen transfer and adsorption capabilities. Besides, two new peaks were observed in Fig. 8d, while the bonds at 1651 cm^{-1} and 1723 cm^{-1} were attributed to -C=C- vibrations of FA [36] and -C-O- stretching vibration of FF [60], respectively. These results further proved that the different adsorption configurations lead to the formation of THFA, and slow down the desorption of the products.

Above all, the mechanism of the quenching coupled oxygen vacancies anchoring method on the structure and activity of the high-entropy catalyst was summarized in Fig. 9. Firstly, it has been proved that the ultra-low loading high-entropy catalyst was prepared via the quenching coupled with oxygen vacancies anchoring method. Combined the quenching and reduction process, the loading metals, especially Zn and Mo, promoted the formation of the surface oxygen vacancies via inducing lattice distortion (Zn doping) or weakening Ti-O (Mo transfer electron). Moreover, the loading metals also induced the phenomena of SMSI, which further enhanced the interaction between HEA and TiO$_2$, while the TiO$_2$ derived SMSI driven encapsulated layer provided abundant oxygen vacancies for absorbing reactant, but also offered the channel for the hydrogen spillover from HEA. Therefore, the catalytic system is fully prepared to achieve efficient conversion of FF, in which the HEA can offer sufficient hydrogen proton and OVs can provide the FF absorption sites and spillover hydrogen space. Then the HEA-TiO$_2$ catalyst showed remarkably high productivity at the ambient temperature (30 °C). Moreover, the intermetallic electron transfer in the HEA adjusted the electron distribution of Pd, resulting in more Pd^0 in the HEA, which provided more hydrogen dissociation sites and decreased the Pd^{2+} proportion. Furthermore, the proportion of Pd^0 and Pd^{2+} also influence the FF adsorption configurations, while the HEA-TiO$_2$ catalyst maintained the vertical FF adsorption configuration, improving the FA
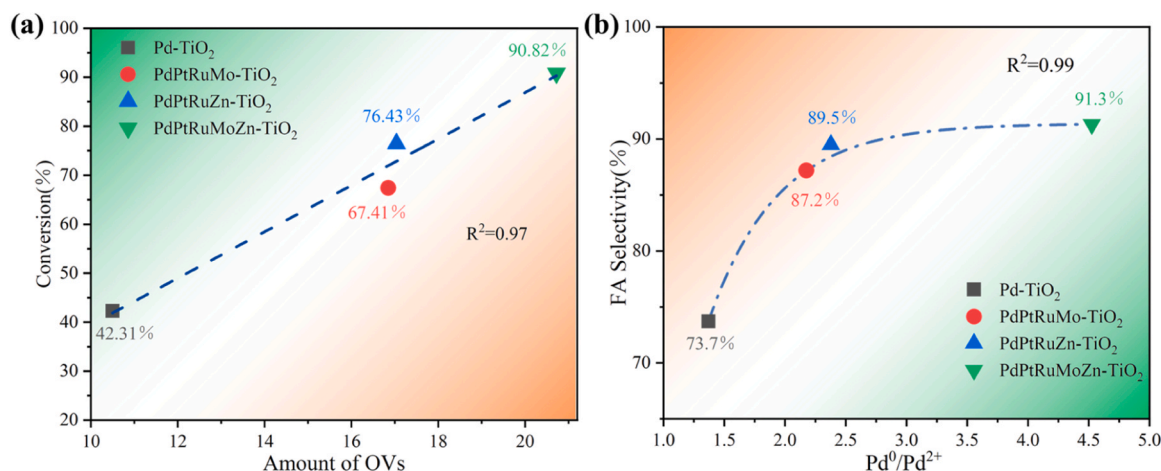

Fig. 7. (a) The correlation between the number of OVs in the catalyst and FF conversion, (b) The correlation between the Pd^0/Pd^{2+} ratio in the catalyst and FA selectivity. Amount of OVs: Obtained by integrating the peak area of EPR.
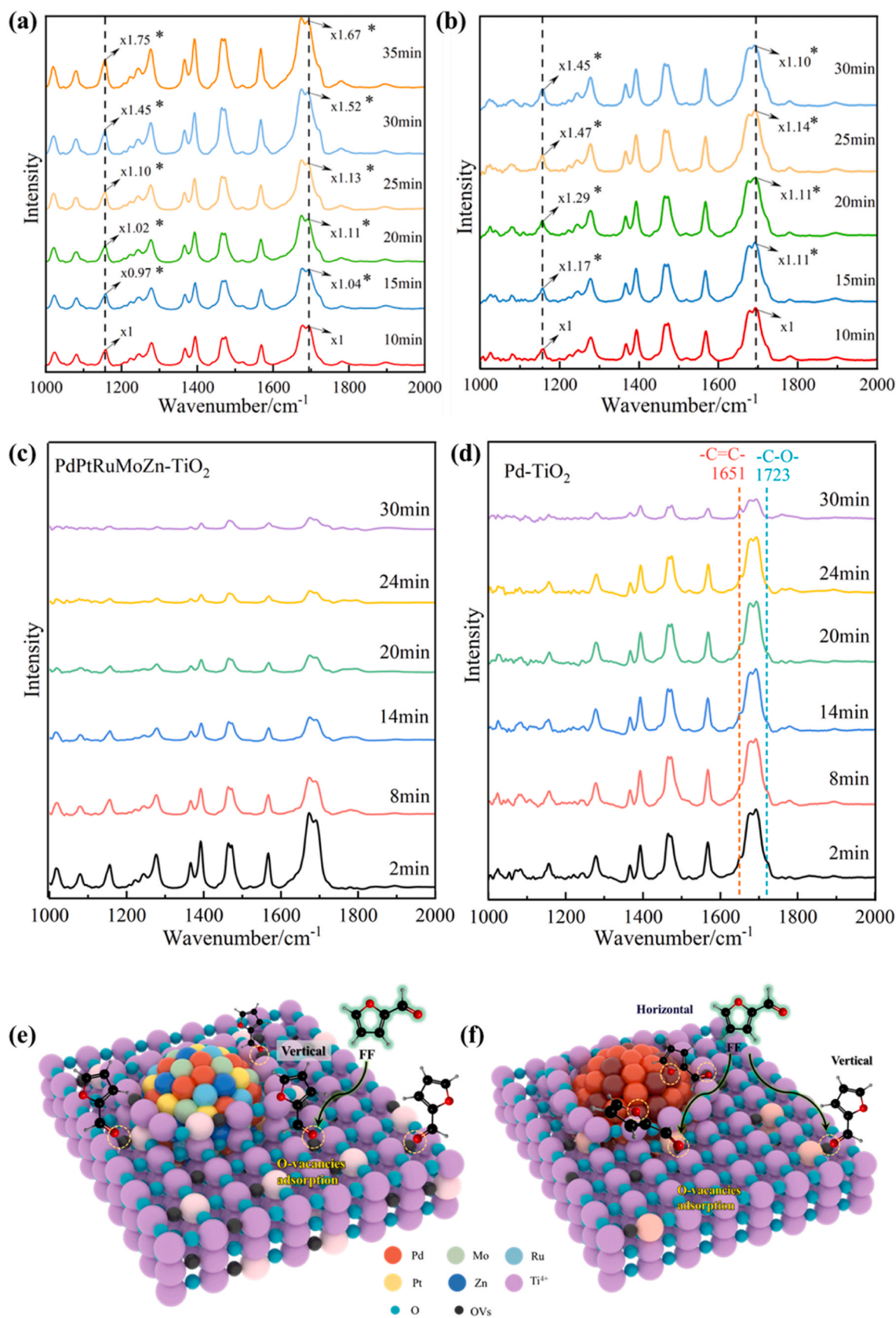
Fig. 8. In situ DRIFTS spectra measured during FF adsorption processes. (a) PdPtRuMoZn-TiO₂ and (b) Pd-TiO₂, * : the ratio of FF adsorption desorption peak area of different time to 10 min. In situ DRIFTS spectra of FF adsorbed samples measured in the hydrogen stream. (c) PdPtRuMoZn-TiO₂ and (d) Pd-TiO₂. Schematic diagram of the adsorption pattern of furfural on different catalysts. (e) PdPtRuMoZn-TiO₂ and (f) Pd-TiO₂.
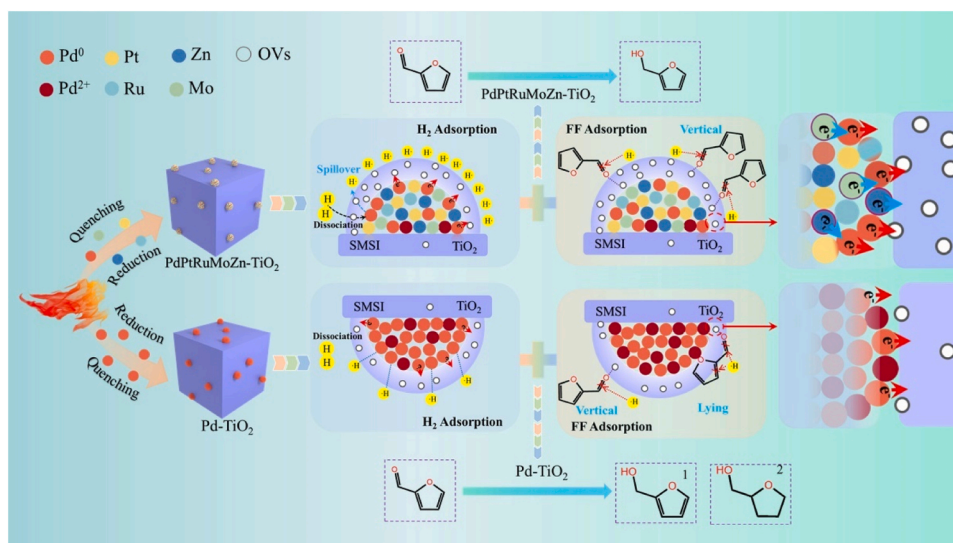
Fig. 9. The comparation of proposed reaction mechanism for FF to FA via the PdPtRuMoZn-TiO$_2$ and Pd-TiO$_2$ catalyst.

selectivity significantly.

4. Conclusion

The ultra-low loading HEA-TiO$_2$ catalysts with SMSI driven encapsulated layer were prepared via the quenching method to achieve the hydrogenation of Furfural at ambient temperature. The results of XRD, EPR, and XPS showed that Mo promoted the transfer of electrons and enhanced the interaction between HEA and TiO$_2$. And Zn doping induced the adjusting of the electronic environment of HEA, obtaining richer oxygen vacancies. Moreover, intermetallic electron transfer in the high-entropy alloy also decreased the horizontal adsorption configuration of FF on the catalyst surface, improving both the FF conversion and FA selectivity (90.82% furfural conversion and 91.3% furfuryl alcohol selectivity) at ambient temperature. This high-entropy alloy catalyst preparation strategy will inspire the design of complex catalysts for important reactions with high effective and multiple sites at ambient temperature.

CRediT authorship contribution statement

Xiwei Xu wrote the first draft of the manuscript. **Hui Yang** carried out all the experiments, analyzed the data. **Ren Tu** performed the analysis of the characterizations' results. **Shuhong Liu, Jingye Hu, Yingnan Li** assisted in solving the problems encountered during the experiment and participated in discussion. **Yan Sun** conceived the idea and supervised the project. All authors reviewed and commented on the manuscript before publication.

Declaration of Competing Interest

We declare that we have no known competing financial interests or personal relationships that could have appeared to influence the work reported in this paper.

Data Availability

No data was used for the research described in the article.

Acknowledgment

Appendix A. Supporting information

Supplementary data associated with this article can be found in the online version at doi:10.1016/j.apcatb.2023.123358.

References

[1] R.H. Liu, H.Y. Chen, K.P. Zhao, Y.T. Qin, B.B. Jiang, T.S. Zhang, G. Sha, X. Shi, C. Uher, W.Q. Zhang, L.D. Chen, Entropy as a gene-Like performance indicator promoting thermoelectric materials, Adv. Mater. 29 (2017) 7, https://doi.org/10.1002/adma.201702712.

[2] Y.F. Sun, S. Dai, High-entropy materials for catalysis: a new frontier, Sci. Adv. 7 (2021), https://doi.org/10.1126/sciadv.abg1600.

[3] N.X. Zhou, S.C. Jiang, T. Huang, M.D. Qin, T. Hu, J. Luo, Single-phase high-entropy intermetallic compounds (HEICs): bridging high-entropy alloys and ceramics, Sci. Bull. 64 (2019) 856–864, https://doi.org/10.1016/j.scib.2019.05.007.

[4] E.P. George, D. Raabe, R.O. Ritchie, High-entropy alloys, Nat. Rev. Matter 4 (2019) 515–534, https://doi.org/10.1038/s41578-019-0121-4.

[5] H. Zhu, S.H. Sun, J.C. Hao, Z.C. Zhuang, S.G. Zhang, T.D. Wang, Q. Kang, S.L. Lu, X.F. Wang, F.L. Lai, T.X. Liu, G.H. Gao, M.L. Du, D.S. Wang, A high-entropy atomic environment converts inactive to active sites for electrocatalysis, Energ. Environ. Sci. 16 (2023) 619–628, https://doi.org/10.1039/d2ee03185j.

[6] L.L. Yu, K.Z. Zeng, C.H. Li, X.R. Lin, H.W. Liu, W.H. Shi, H.J. Qiu, Y.F. Yuan, Y.G. Yao, High-entropy alloy catalysts: from bulk to nano toward highly efficient carbon and nitrogen catalysis, Carbon Energy 4 (2022) 731–761, https://doi.org/10.1002/cey2.228.

[7] D. Zhang, H. Zhao, X.K. Wu, Y. Deng, Z.C. Wang, Y. Han, H.D. Li, Y. Shi, X.L. Chen, S.X. Li, J.P. Lai, B.L. Huang, L. Wang, Multi-site electrocatalysts boost ph-universal nitrogen reduction by high-entropy alloys, Adv. Funct. Mater. 31 (2021) 8, https://doi.org/10.1002/adfm.202006939.

[8] H.D. Li, Y. Han, H. Zhao, W.J. Qi, D. Zhang, Y.D. Yu, W.W. Cai, S.X. Li, J.P. Lai, B.L. Huang, L. Wang, Fast site-to-site electron transfer of high-entropy alloy nanocatalyst driving redox electrocatalysis, Nat. Commun. 11 (2020) 9, https://doi.org/10.1038/s41467-020-19277-9.

[9] R. Tu, K.L. Liang, Y. Sun, Y.W. Wu, W. Lv, C.Q. Jia, E.C. Jiang, Y.J. Wu, X.D. Fan, B. Zhang, Q. Lu, B.S. Zhang, X.W. Xu, Ultra-dilute high-entropy alloy catalyst with core-shell structure for high-active hydrogenation of furfural to furfuryl alcohol at mild temperature, Chem. Eng. J. 452 (2023) 11, https://doi.org/10.1016/j.cej.2022.139526.

[10] P.F. Xie, Y.G. Yao, Z.N. Huang, Z.Y. Liu, J.L. Zhang, T.Y. Li, G.F. Wang, R. Shahbazian-Yassar, L.B. Hu, C. Wang, Highly efficient decomposition of ammonia using high-entropy alloy catalysts, Nat. Commun. 10 (2019) 12, https://doi.org/10.1038/s41467-019-11848-9.

[11] Y.G. Yao, Z.N. Huang, P.F. Xie, S.D. Lacey, R.J. Jacob, H. Xie, F.J. Chen, A.M. Nie, T.C. Pu, M. Rehwoldt, D.W. Yu, M.R. Zachariah, C. Wang, R. Shahbazian-Yassar, J. Li, L.B. Hu, Carbothermal shock synthesis of high-entropy-alloy nanoparticles, Science 359 (2018) 1489–1494, https://doi.org/10.1126/science.aan5412.

[12] Q. Dong, Y.G. Yao, S.C. Cheng, K. Alexopoulos, J.L. Gao, S. Srinivas, Y.F. Wang, Y. Pei, C.L. Zheng, A.H. Brozena, H. Zhao, X.Z. Wang, H.E. Toraman, B. Yang, I. G. Kevrekidis, Y.G. Ju, D.G. Vlachos, D.X. Liu, L.B. Hu, Programmable heating and quenching for efficient thermochemical synthesis, Nature 605 (2022) 470–476, https://doi.org/10.1038/s41586-022-04568-6.

[13] M.W. Glasscott, J.E. Dick, Fine-tuning porosity and time-resolved observation of the nucleation and growth o single platinum nanoparticles, ACS Nano 13 (2019) 4572–4581, https://doi.org/10.1021/acsnano.9b00546.

[14] C.C. Ye, J.Z. Liu, Q.H. Zhang, X.J. Jin, Y. Zhao, Z.H. Pan, G.X. Chen, Y.C. Qiu, D. Q. Ye, L. Gu, G.I.N. Waterhouse, L. Guo, S.H. Yang, Activating metal oxides nanocatalysts for electrocatalytic water oxidation by quenching-induced near-surface metal atom functionality, J. Am. Chem. Soc. 143 (2021) 14169–14177, https://doi.org/10.1021/jacs.1c04737.

[15] D.S. Wu, K. Kusada, T. Yamamoto, T. Toriyama, S. Matsumura, S. Kawaguchi, Y. Kubota, H. Kitagawa, Platinum-group-metal high-entropy-alloy nanoparticles, J. Am. Chem. Soc. 142 (2020) 13833–13838, https://doi.org/10.1021/jacs.0c04807.

[16] Y.G. Yao, Q. Dong, A. Brozena, J. Luo, J.W. Miao, M.F. Chi, C. Wang, I. G. Kevrekidis, Z.J. Ren, J. Greeley, G.F. Wang, A. Anapolsky, L.B. Hu, High-entropy nanoparticles: synthesis-structure-property relationships and data-driven discovery, Science 376 (2022) 151, https://doi.org/10.1126/science.abn3103.

[17] H.O. Otor, J.B. Steiner, C. Garcia-Sancho, A.C. Alba-Rubio, Encapsulation methods for control of catalyst deactivation: A review, ACS Catal. 10 (2020) 7630–7656, https://doi.org/10.1021/acscatal.0c01569.

[18] R.H. Li, Z.Q. Liu, Q.T. Trinh, Z.Q. Miao, S. Chen, K.C. Qian, R.J. Wong, S.B. Xi, Y. Yan, A. Borgna, S.P. Liang, T. Wei, Y.H. Dai, P. Wang, Y. Tang, X.Q. Yan, T. S. Choksi, W. Liu, Strong metal-support interaction for 2D materials: Application in noble metal/TiB₂ heterointerfaces and their enhanced catalytic performance for formic acid dehydrogenation, Adv. Mater. 33 (2021) 13, https://doi.org/10.1002/adma.202101536.

[19] Y. Yang, K. Xu, X.L. Ma, Catalytic mechanism of oxygen vacancy defects in metal oxides, Prog. Chem. 35 (2023) 543–559, https://doi.org/10.7536/pc221122.

[20] A. Beniya, S. Higashi, Towards dense single-atom catalysts for future automotive applications, Nat. Catal. 2 (2019) 590–602, https://doi.org/10.1038/s41929-019-0282-y.

[21] L. Nie, D. Mei, H. Xiong, B. Peng, Z. Ren, X.I.P. Hernandez, A. DeLaRiva, M. Wang, M.H. Engelhard, L. Kovarik, A.K. Datye, Y. Wang, Activation of surface lattice oxygen in single-atom Pt/CeO₂ for low-temperature CO oxidation, Science 363 (2019) 1419–1423, https://doi.org/10.1126/science.aaw5872.

[22] P. Sudarsanam, E. Peeters, E.V. Makshina, V.I. Parvulescu, B.F. Sels, Advances in porous and nanoscale catalysts for viable biomass conversion, Chem. Soc. Rev. 48 (2019) 2366–2421, https://doi.org/10.1039/c8cs00452h.

[23] L.T. Mika, E. Csefalvay, A. Nemeth, Catalytic conversion of carbohydrates to initial platform chemicals: chemistry and sustainability, Chem. Rev. 118 (2018) 505–613, https://doi.org/10.1021/acs.chemrev.7b00395.

[24] J. Gupta, K. Papadikis, E.Y. Konysheva, Y. Lin, I.V. Kozhevnikov, J. Li, CaO catalyst for multi-route conversion of oakwood biomass to value-added chemicals and fuel precursors in fast pyrolysis, Appl. Catal. B 285 (2021), 119858, https://doi.org/10.1016/j.apcatb.2020.119858.

[25] S. Wang, A. Cheng, F. Liu, J. Zhang, T. Xia, X. Zeng, W. Fan, Y. Zhang, Catalytic conversion network for lignocellulosic biomass valorization: a panoramic view, Ind. Chem. Mater. (2023), https://doi.org/10.1039/D2IM00054G.

[26] C.Y. Yang, C.F. Zhuang, Z.X. Zhai, X. Zhao, D.J. Huang, D. Tian, C.G. Min, J. Zhao, Y. Wang, Phase regulation of Ni-based catalyst promotes selective hydrogenation of furfural: effect of glycerol and Zn content, Appl. Catal. B 334 (2023), https://doi.org/10.1016/j.apcatb.2023.122854.

[27] Z. Mukadam, S.H. Liu, A. Pedersen, J. Barrio, S. Fearn, S.C. Sarma, M.M. Titirici, S. B. Scott, I.E.L. Stephens, K.R. Chan, S. Mezzavilla, Furfural electrovalorisation using single-atom molecular catalysts, Energ. Environ. Sci. 16 (2023) 2934–2944, https://doi.org/10.1039/d3ee00551h.

[28] M.J. Taylor, L. Jiang, J. Reichert, A.C. Papageorgiou, S.K. Beaumont, K. Wilson, A. F. Lee, J.V. Barth, G. Kyriakou, Catalytic hydrogenation and hydrodeoxygenation of furfural over Pt(111): a model system for the rational design and operation of practical biomass conversion catalysts, J. Phys. Chem. C 121 (2017) 8490–8497, https://doi.org/10.1021/acs.jpcc.7b01744.

[29] M.J. Islam, M. Granollers Mesa, A. Osatiashtiani, M.J. Taylor, J.C. Manayil, C.M. A. Parlett, M.A. Isaacs, G. Kyriakou, The effect of metal precursor on copper phase dispersion and nanoparticle formation for the catalytic transformations of furfural, Appl. Catal. B 273 (2020), 119062, https://doi.org/10.1016/j.apcatb.2020.119062.

[30] Z.X. Lin, W.M. Wan, S.Y. Yao, J.G.G. Chen, Cobalt-modified molybdenum carbide as a selective catalyst for hydrodeoxygenation of furfural, Appl. Catal. B 233 (2018) 160–166, https://doi.org/10.1016/j.apcatb.2018.03.113.

[31] W. Ahmad, H. Jeong, H.H. Nahm, Y. Lee, E. Park, H. Lee, G. Ali, Y.H. Kim, J. Jurng, Y. Oh, Metal-anchoring, metal oxidation-resistance, and electron transfer behavior of oxygen vacancy-rich TiO₂ in supported noble metal catalyst for room temperature HCHO conversion, Chem. Eng. J. 467 (2023), https://doi.org/10.1016/j.cej.2023.143412.

[32] L. Li, Z.D. Wei, Y. Zhang, X.Q. Qi, M.R. Xia, J. Zhang, Z.G. Shao, C.X. Sun, DFT study of difference caused by catalyst supports in Pt and Pd catalysis of oxygen reduction reaction, Sci. China Ser. B. 52 (2009) 571–578, https://doi.org/10.1007/s11426-009-0006-2.

[33] A.P. Tsai, S. Kameoka, K. Nozawa, M. Shimoda, Y. Ishii, Intermetallic: A pseudoelement for catalysis published as part of the accounts of chemical research special issue "Advancing chemistry through intermetallic compounds", Acc. Chem. Res 50 (2017) 2879–2885, https://doi.org/10.1021/acs.accounts.7b00476.

[34] S.L. Wang, K.G. Gao, W. Li, J.L. Zhang, Effect of Zn addition on the direct synthesis of hydrogen peroxide over supported palladium catalysts, Appl. Catal. A 531 (2017) 89–95, https://doi.org/10.1016/j.apcata.2016.10.023.

[35] V. Kumaravel, S. Rhatigan, S. Mathew, M.C. Michel, J. Bartlett, M. Nolan, S. J. Hinder, A. Gasco, C. Ruiz-Palomar, D. Hermosilla, S.C. Pillai, Mo doped TiO₂: impact on oxygen vacancies, anatase phase stability and photocatalytic activity, J. Phys. Mater. 3 (2020), https://doi.org/10.1088/2515-7639/ab749c.

[36] X.L. Qing, L. Yuan, C. Wang, M. Bi, Y.Q. Wang, X.L. Weng, Structural and visible-near infrared optical properties of (Fe, Mo)-co-doped TiO2 for colored cool pigments, J. Alloy. Compd. 826 (2020) 9, https://doi.org/10.1016/j.jallcom.2020.153946.

[37] L.H. Li, L.L. Yu, Z.Y. Lin, G.W. Yang, Reduced TiO2-graphene oxide heterostructure as broad spectrum-driven efficient water-splitting photocatalysts, ACS Appl. Mater. Interfaces 8 (2016) 8536–8545, https://doi.org/10.1021/acsami.6b00966.

[38] C.S. Guan, T. Hou, W.Y. Nie, Q. Zhang, L.B. Duan, X.R. Zhao, Enhanced photocatalytic reduction of CO2 on BiOBr under synergistic effect of Zn doping and induced oxygen vacancy generation, J. Colloid Interface Sci. 633 (2023) 177–188, https://doi.org/10.1016/j.jcis.2022.11.106.

[39] K.Q. Jing, Y.Q. Fu, Z.Q. Wang, Z.N. Chen, H.Z. Tan, J. Sun, Z.N. Xu, G.C. Guo, Zn²⁺ stabilized Pd clusters with enhanced covalent metal-support interaction via the formation of Pd-Zn bonds to promote catalytic thermal stability, Nanoscale 12 (2020) 14825–14830, https://doi.org/10.1039/d0nr02987d.

[40] J. Zhang, L.Q. Chen, Y.X. Fan, C. Zhao, W.L. Dai, L.X. Yang, L. Zhou, J.P. Zou, X. B. Luo, Unraveling the high catalytic activity of single atom Mo-doped TiO₂ toward NH₃-SCR: synergetic roles of Mo as acid sites and oxygen vacancies as oxidation sites, Chem. Eng. J. 465 (2023), https://doi.org/10.1016/j.cej.2023.142759.

[41] J. Zhang, M.L. Zou, Q. Li, W.L. Dai, D. Wang, S.Q. Zhang, B. Li, L.X. Yang, S.L. Luo, X.B. Luo, Thermally activated construction of open metal sites on a Zn-organic framework: an effective strategy to enhance Lewis acid properties and catalytic performance for CO2 cycloaddition reactions, Appl. Surf. Sci. 572 (2022), https://doi.org/10.1016/j.apsusc.2021.151408.

[42] Y.Y. Zhan, C. Zhou, F. Jin, C.Q. Chen, L.L. Jiang, Ru/TiO2 catalyst for selective hydrogenation of benzene: effect of surface hydroxyl groups and spillover hydrogen, Appl. Surf. Sci. 525 (2020), https://doi.org/10.1016/j.apsusc.2020.146627.

[43] J.Y. Jin, S.Z. Hu, X.S. Zhang, S.G. Sun, Effect of MoO3 on Pd nanoparticles for efficient formic acid electrooxidation, Int. J. Hydrog. Energy 48 (2023) 15483–15491, https://doi.org/10.1016/j.ijhydene.2022.10.134.

[44] J. Wei, S.N. Qin, J.L. Liu, X.Y. Ruan, Z.Q. Guan, H. Yan, D.Y. Wei, H. Zhang, J. Cheng, H.X. Xu, Z.Q. Tian, J.F. Li, In situ raman monitoring and manipulating of interfacial hydrogen spillover by precise fabrication of Au/TiO2/Pt sandwich structures, Angew. Chem. -Int. Ed. 59 (2020) 10343–10347, https://doi.org/10.1002/anie.202000426.

[45] B. Wang, X.H. Wang, L. Lu, C.G. Zhou, Z.Y. Xi, J.J. Wang, X.K. Ke, G.D. Sheng, S. C. Yan, Z.G. Zou, Oxygen-vacancy-activated CO2 splitting over amorphous oxide semiconductor photocatalyst, ACS Catal. 8 (2018) 516–525, https://doi.org/10.1021/acscatal.7b02952.

[46] S.O. Wu, K.Y. Tseng, R. Kato, T.S. Wu, A. Large, Y.K. Peng, W.K. Xiang, H.H. Fang, J.Y. Mo, I. Wilkinson, Y.L. Soo, G. Held, K. Suenaga, T. Li, H.Y.T. Chen, S.C. E. Tsang, Rapid interchangeable hydrogen, hydride, and proton species at the interface of transition metal atom on oxide surface, J. Am. Chem. Soc. 143 (2021) 9105–9112, https://doi.org/10.1021/jacs.1c02859.

[47] D. Wu, Y. Kang, F. Wang, J. Yang, Y. Xu, Y. Zhuang, J. Wu, J. Zeng, Y. Yang, J. Zhao, Surface-redox pseudocapacitance-dominated charge storage mechanism enabled by the reconstructed cathode/electrolyte interface for high-rate magnesium batteries, Adv. Energy Mater. 13 (2023), 2301145, https://doi.org/10.1002/aenm.202301145.

[48] G. Gao, J. Remon, Z.C. Jiang, L. Yao, C.W. Hu, Selective hydrogenation of furfural to furfuryl alcohol in water under mild conditions over a hydrotalcite-derived Pt-based catalyst, Appl. Catal. B 309 (2022), https://doi.org/10.1016/j.apcatb.2022.121260.

[49] X. Song, F.J. Shao, Z.J. Zhao, X.N. Li, Z.Z. Wei, J.G. Wang, Mg-modified Al₂O₃ regulates the supported Pd with Pd0/Pd²⁺ ratio for 2-butyn-l-ol semi-hydrogenation performance, Chem. Eng. Sci. 274 (2023), https://doi.org/10.1016/j.ces.2023.118609.

[50] A.B. Merlo, V. Vetere, J.F. Ruggera, M.L. Casella, Bimetallic PtSn catalyst for the selective hydrogenation of furfural to furfuryl alcohol in liquid-phase, Catal. Commun. 10 (2009) 1665–1669, https://doi.org/10.1016/j.catcom.2009.05.005.

[51] O.F. Aldosari, S. Iqbal, P.J. Miedziak, G.L. Brett, D.R. Jones, X. Liu, J.K. Edwards, D.J. Morgan, D.K. Knight, G.J. Hutchings, Pd-Ru/TiO2 catalyst - an active and selective catalyst for furfural hydrogenation, Catal. Sci. Technol. 6 (2016) 234–242, https://doi.org/10.1039/c5cy01650a.

[52] M. Jun, H. Kang, D. Kim, G.J. Bang, M. Kim, H. Jin, T. Kwon, H. Baik, J.H. Sohn, Y. Jung, H. Kim, K. Lee, Pd3Pb nanosponges for selective conversion of furfural to furfuryl alcohol under mild condition, Small Methods 5 (2021), https://doi.org/10.1002/smtd.202100400.

[53] S.T. Thompson, H.H. Lamb, Palladium-Rhenium catalysts for selective hydrogenation of furfural: evidence for an optimum surface composition, ACS Catal. 6 (2016) 7438–7447, https://doi.org/10.1021/acscatal.6b01398.

[54] M.M. Villaverde, N.M. Bertero, T.F. Garetto, A.J. Marchi, Selective liquid-phase hydrogenation of furfural to furfuryl alcohol over Cu-based catalysts, Catal. Today 213 (2013) 87–92, https://doi.org/10.1016/j.cattod.2013.02.031.

[55] R.V. Sharma, U. Das, R. Sammynaiken, A.K. Dalai, Liquid phase chemo-selective catalytic hydrogenation of furfural to furfuryl alcohol, Appl. Catal. A 454 (2013) 127–136, https://doi.org/10.1016/j.apcata.2012.12.010.

[56] S.J. Li, Y.F. Fan, C.H. Wu, C.F. Zhuang, Y. Wang, X.M. Li, J. Zhao, Z.F. Zheng, Selective hydrogenation of furfural over the Co-based catalyst: a subtle synergy with Ni and Zn dopants, ACS Appl. Mater. Interfaces 13 (2021) 8507–8517, https://doi.org/10.1021/acsami.1c01436.

[57] Y.F. Fan, S.J. Li, Y. Wang, C.F. Zhuang, X.T. Liu, G.S. Zhu, X.Q. Zou, Tuning the synthesis of polymetallic-doped ZIF derived materials for efficient hydrogenation of furfural to furfuryl alcohol, Nanoscale 12 (2020) 18296–18304, https://doi.org/10.1039/d0nr04098c.

[58] M.J. Islam, M.G. Mesa, A. Osatiashtiani, J.C. Manayil, M.A. Isaacs, M.J. Taylor, S. Tsatsos, G. Kyriakou, PdCu single atom alloys supported on alumina for the selective hydrogenation of furfural, Appl. Catal. B 299 (2021), https://doi.org/10.1016/j.apcatb.2021.120652.

[59] Z.X. Zhai, J. Chu, L. Sun, X. Zhao, D.J. Huang, X.Q. Yang, C.F. Zhuang, C.A. Min, Y. Wang, Ultrahigh metal content carbon-based catalyst for efficient hydrogenation of furfural: the regulatory effect of glycerol, ACS Appl. Mater. Interfaces 14 (2022) 44439–44449, https://doi.org/10.1021/acsami.2c12874.

[60] C.H. Liang, H.X. Li, M. Peng, X.Q. Zhang, Q.K. Jiang, J. Cui, Y.J. Ding, Z.C. Zhang, Co decorated low Pt loading nanoparticles over TiO$_2$ catalyst for selective hydrogenation of furfural, Appl. Catal. A 643 (2022) 11, https://doi.org/10.1016/j.apcata.2022.118766.